

Banner appropriate to article type will appear here in typeset article

Effect of Reynolds number on triboelectric particle charging in turbulent channel flow

Christoph Wilms^{1,2} and Holger Grosshans^{1,2}

¹Physikalisch-Technische Bundesanstalt, Bundesallee 100, Braunschweig, Germany

²Otto von Guericke University Magdeburg, Universitätsplatz 2, Magdeburg, Germany

Corresponding author: Christoph Wilms, Christoph.Wilms@ptb.de

(Received xx; revised xx; accepted xx)

Triboelectric charging in particle-laden flows is a complex interplay of fluid and particle dynamics, collision mechanics, and electrostatics. In this study, we introduce triboFoam, an open-source solver built on the OpenFOAM framework, designed to simulate triboelectric charging in particle-laden turbulent flows. We validate triboFoam using Direct Numerical Simulations (DNS) of a fully developed turbulent channel flow at a friction Reynolds number of $Re_\tau = 180$. The results demonstrate good agreement with DNS data for particle concentration profiles and charge distributions. Then, we investigate the influence of Reynolds number on particle distribution and charging behaviour using Large-Eddy Simulations (LES) at varying friction Reynolds numbers up to $Re_\tau = 550$. Our findings reveal that higher Reynolds numbers lead to increased near-wall particle concentrations and enhanced charging rates, attributed to intensified turbulent fluctuations and elevated impact velocities. Finally, an empirical correlation is proposed to predict the average particle charging rate as a function of Reynolds number and particle diameter. With this work, we provide a tool for simulating triboelectric charging in complex geometries and turbulent flows, advancing the understanding of electrostatic phenomena in particle-laden systems. The empirical correlation offers practical insights for predicting charging behaviour in industrial applications and thus can contribute to improved safety and efficiency in processes involving particulate matter.

1. Introduction

During the handling of polymers, pharmaceuticals, food, and other powdered materials, particles frequently become electrified via triboelectric (frictional) charging. Electrostatic charge can result in many undesirable effects, such as particle segregation, adhesion, fouling, blockages of pipes, reduced system efficiency, and even dust explosions (Giffin & Mehrani 2013; Oshawa 2011). Many industrial dust explosions have been attributed to the discharge of static electricity, for example, when filling silos with fine powders and high particle throughput (Glor 2001; Nifuku & Katoh 2003; Zhang *et al.* 2026). Among all powder handling operations, including sieving, pouring, and grinding, the

highest charge appears in pneumatic conveying, where the particles are transported by a highly turbulent flow (Glor 1985). Understanding the mechanisms governing triboelectric charging in turbulent particle-laden flows is therefore essential for the design of safe and efficient industrial processes.

Experiments have shown that flow velocity, i.e., Reynolds number, is one of the most important and controllable parameters affecting particle charging and, hence, the hazard of dust explosions (Schwindt *et al.* 2017; Fath *et al.* 2013). However, most numerical investigations using Direct Numerical Simulations (DNS) have focused, to reduce computational costs, on the low-turbulent regime with a friction Reynolds number of $Re_\tau = 180$ or lower (Grosshans & Papalexandris 2017a; Ozler & Grosshans 2025; Jin & Marshall 2017). Investigations at higher Reynolds numbers ($Re_\tau \approx 550$) showed significant influence of the particle concentration profiles. Nonetheless, the Reynolds number was fixed. As the particle charge was prescribed and constant, its influence on charging was not investigated (Zhang *et al.* 2023; Cui *et al.* 2024).

The few available numerical studies regarding the effect of Reynolds number on triboelectric charging have reported contradictory results. Tanoue *et al.* (2001) observed in Reynolds-averaged Navier-Stokes (RANS) simulations a decrease in charge with increasing Reynolds number. Contrary, Watano (2006) found no significant dependence in Discrete Element Modelling (DEM) simulations, and the Large-Eddy Simulations (LES) by Grosshans & Papalexandris (2016a) showed an increase in charge with increasing Reynolds number. Clarifying these discrepancies requires a systematic investigation of how different Reynolds numbers affect the particle distribution and charging rate.

Advances in computational resources over the past decades have made it feasible to simulate triboelectric charging in increasingly complex systems. Coupled computational fluid dynamics–discrete element method (CFD–DEM) approaches have become a common tool to investigate triboelectric charging at the fundamental level, as they allow for the coupling of the carrier flow dynamics with the motion of individual particles, including electrostatic interactions. Since particles acquire most of their charge during collisions and collision dynamics are strongly influenced by the surrounding flow, accurate modelling of the fluid phase is crucial.

Early RANS simulations (Tanoue *et al.* 2001) model all turbulent motions. More recent LES resolve the large-scale turbulent structures in space and time (Grosshans & Papalexandris 2016b; Korevaar *et al.* 2014; Grosshans & Papalexandris 2016a). In these LES (Grosshans & Papalexandris 2016a), the increase in the air velocity led to intensified turbulent fluctuations and thereby increased wall-normal particle velocities, impact velocities, and effective contact areas during collisions. However, these LES did not resolve the viscous sub- and buffer layer, although this region exhibits the highest turbulence intensities and strongest velocity gradients, which can strongly influence charging. Furthermore, particle–particle collisions were neglected (Grosshans & Papalexandris 2016a), even though they may significantly affect the particle distribution, even in dilute regimes (Rupp *et al.* 2023). Resolving all turbulent scales, DNS revealed that triboelectric charging is strongly affected by small-scale motions (Grosshans & Papalexandris 2017a; Jantač & Grosshans 2024). Reliable prediction of charging in particle-laden turbulent flows, therefore, requires DNS or LES with a resolved viscous sublayer. However, the high computational cost of DNS limits such studies to low Reynolds numbers and simple geometries, such as channels, ducts, or straight pipes.

From an industrial perspective, flows at high Reynolds numbers are of particular relevance. Pneumatic conveying systems operating in the dilute regime typically employ air velocities in the range of 10 m s^{-1} to 30 m s^{-1} , which, for a pipe diameter of 0.1 m, correspond to Reynolds numbers of order $Re = O(10^5)$ (Klinzing 2018; Jones 1997).

This range underscores the need to investigate triboelectric charging at higher Reynolds numbers than those addressed in previous DNS, as both mixing processes and turbulence characteristics undergo pronounced changes with increasing Reynolds number (Lee & Moser 2015).

Also, complex geometries are particularly relevant for industrial applications, as most conveying systems comprise pipe bends, contractions, expansions, and junctions. These features can strongly influence charging behaviour due to increased impact velocities and contact areas with the walls. For example, Yan *et al.* (2021) showed that electrostatic forces enhance particle accumulation in the near-wall region of bends, which may increase particle-wall collision frequency and thus charge transfer.

To isolate and quantify the influence of Reynolds number, investigations at different fixed Reynolds numbers are essential. In this context, fully developed conditions of both the gas and particle phases are favoured, as they eliminate spatial transients and allow changes in charging behaviour to be attributed unambiguously to Reynolds-number effects. Numerical simulations offer a clear advantage in this regard. In experimental configurations, it is essentially impossible to establish a fully developed state of both phases without simultaneously inducing particle charging. Therefore, reproducibility in experiments is challenging because it is difficult to control the electrostatic boundary conditions (Lim *et al.* 2006). Moreover, achieving such conditions would require very long ducts, preferably oriented vertically to minimise gravitational segregation within the cross-section, rendering systematic parametric studies impractical. In contrast, numerical simulations can employ periodic boundary conditions to fully developed the flow within a compact computational domain.

To date, the only open-source code for simulating triboelectric particle charging (Grosshans *et al.* 2026) is limited to simple geometries, namely channels and rectangular ducts, and lacks turbulence models. To overcome these limitations, we introduce in this paper a new open-source solver, triboFoam (Wilms & Grosshans 2026). This new solver is built upon OpenFOAM (Weller *et al.* 1998) and, thus, takes advantage of the framework's capabilities to model turbulence and complex geometries. In the present work, we apply LES with a fully resolved viscous sublayer to simulate friction Reynolds numbers up to $Re_\tau = 550$, ensuring sufficient numerical resolution. In addition, different particle diameters are investigated to assess the influence of particle inertia in interaction with turbulent structures.

The remainder of the paper is organised as follows. Section 2 presents the governing equations of the fluid and particle phase, including the electrostatic and charging models. Section 3 describes the numerical setup of the DNS and LES simulations, followed by Section 4 presenting and discussing the results. Finally, conclusions are drawn in Section 5.

2. Mathematical modeling

The system is modelled using an Eulerian framework for the fluid phase and a Lagrangian framework to capture the particle motion. In this approach, the flow is considered to be dilute, meaning that the volume occupied by the particles is very small compared to the fluid volume, which allows us to consider the particles as point quantities.

2.1. Fluid phase

The fluid phase is described by the incompressible Navier-Stokes equations with constant diffusivities,

$$\nabla \cdot \mathbf{u} = 0 \quad (2.1a)$$

and

$$\frac{\partial \mathbf{u}}{\partial t} + (\mathbf{u} \cdot \nabla) \mathbf{u} = -\frac{1}{\rho} \nabla p + \nu \nabla^2 \mathbf{u} + \mathbf{F}_s + \mathbf{F}_f. \quad (2.1b)$$

In these equations, $\mathbf{u} = (u, v, w)$ represents the fluid velocity vector, p the pressure, t the time and the fluid density and kinematic viscosity is described by ρ and ν , respectively. The source term \mathbf{F}_s considers the momentum transfer from the particles to the fluid by summing up all aerodynamic forces over a control volume. The last source term, \mathbf{F}_f , describes a general force acting on the entire fluid, which is, e.g., in the case of a cyclic channel flow, a pressure gradient to propel the flow.

The governing equations of the LES are comparable to those of the DNS. The velocity field of the continuous phase can be decomposed into a filtered component ($\bar{\mathbf{u}}$) and a sub-filter (or sub-grid scale, SGS) component. The filtered Navier-Stokes equations read,

$$\nabla \cdot \bar{\mathbf{u}} = 0 \quad (2.2a)$$

$$\frac{\partial \bar{\mathbf{u}}}{\partial t} + (\bar{\mathbf{u}} \cdot \nabla) \bar{\mathbf{u}} = -\frac{1}{\rho} \nabla \bar{p} + \nu \nabla^2 \bar{\mathbf{u}} - \nabla \cdot \boldsymbol{\tau}_{\text{SGS}} + \mathbf{F}_s \quad (2.2b)$$

with the SGS stress tensor $\boldsymbol{\tau}_{\text{SGS}}$. The equations of motion are closed by a model for the SGS stress tensor. Common models rely on the eddy-viscosity approach, where the SGS tensor is expressed as

$$\boldsymbol{\tau}_{\text{SGS}} - \frac{2}{3} k_{\text{SGS}} \mathbf{I} = -2 \nu_{\text{SGS}} \bar{\mathbf{S}} \quad (2.3)$$

with the sub-grid scale eddy viscosity ν_{SGS} , the sub-grid scale turbulent kinetic energy k_{SGS} the identity tensor \mathbf{I} , and the strain rate tensor $\bar{\mathbf{S}}$, which is defined as

$$\bar{\mathbf{S}} = \frac{1}{2} \left(\nabla \mathbf{u} + (\nabla \mathbf{u})^T \right). \quad (2.4)$$

To close equation (2.3), OpenFOAM provides several subgrid-scale models, namely the Smagorinsky (1963) model, the k -equation model (Yoshizawa 1986), the dynamic k -equation model (Won-Wook & Suresh 1995), and the Wall Adapting Local Eddy-viscosity (WALE) model (Nicoud & Ducros 1999). Section B presents a comparison of these four LES models and shows that, in terms of both velocity profiles and particle distributions, the WALE model matches the DNS results the closest. Consequently, it is adopted as the default SGS model for all subsequent simulations. The WALE model computes the subgrid viscosity proportional to the cube of the wall-normal distance and allows it to vanish in the vicinity of solid walls. The SGS viscosity is given by

$$\nu_{\text{SGS}} = (c_w \mathcal{A})^2 \frac{(\mathbf{S}^d : \mathbf{S}^d)^{3/2}}{\left(\bar{\mathbf{S}} : \bar{\mathbf{S}} \right)^{5/2} + (\mathbf{S}^d : \mathbf{S}^d)^{5/4}} \quad (2.5)$$

with the model constant $c_w = 0.325$, the filter width $\mathcal{A} = \mathcal{V}^{1/3}$, with the cell volume \mathcal{V} , and the traceless symmetric part of the square of the velocity gradient tensor

$$\mathbf{S}^d = \frac{1}{2} \left((\nabla \bar{\mathbf{u}})^2 + \left((\nabla \bar{\mathbf{u}})^2 \right)^T \right) - \frac{1}{3} \text{tr} \left((\nabla \bar{\mathbf{u}})^2 \right) \mathbf{I}. \quad (2.6)$$

2.2. Particle phase

The particle phase is assumed to be an ensemble of multiple rigid and spherical particles made out of the same material with the same density ρ_p . The motion of the particles can

be described by Newton's law,

$$\frac{d\mathbf{u}_p}{dt} = \mathbf{f}_{ad} + \mathbf{f}_{coll} + \mathbf{f}_g + \mathbf{f}_{el} \quad (2.7)$$

with the particle velocity vector \mathbf{u}_p and the specific forces \mathbf{f}_{ad} , \mathbf{f}_{coll} , \mathbf{f}_g , and \mathbf{f}_{el} due to aerodynamics, collisions, gravity, and the electric field, respectively.

We considered in our simulations only the drag force, as it has the highest contribution across all aerodynamic forces. It is computed by (Crowe *et al.* 2011)

$$\mathbf{f}_{ad} = \frac{3}{4} \frac{\rho v C_D Re_p}{\rho_p d_p^2} \quad (2.8)$$

with the particle Reynolds number $Re_p = (|\mathbf{u}_{rel}| d_p) / v$, the particle velocity relative to the fluid velocity $\mathbf{u}_{rel} = \mathbf{u}_p - \mathbf{u}$, the particle density ρ_p , and the particle diameter d_p . The particle drag coefficient (C_D) is a function of Re_p , computed by (Schiller & Naumann 1933)

$$C_D = \begin{cases} \frac{24}{Re_p} \left(1 + \frac{1}{6} Re_p^{2/3} \right) & \text{for } Re_p \leq 1000 \\ 0.424 & \text{for } Re_p > 1000. \end{cases} \quad (2.9)$$

In the following, quantities with subscript w refer to the wall, with subscript i to a particle contacting a wall, and with subscript ij to a particle contacting another particle. The subscript ji is used accordingly to indicate the second particle in a particle-particle collision. To shorten the notation, the subscript p indicates that the particle phase is partially omitted in the following equations. The collision forces can be distinguished into binary particle-particle collisions and particle-wall collisions. In both cases, a hard-sphere model with fully elastic collisions is considered. In particle-wall collisions, the wall-normal velocity component flips its sign while the wall-tangential components remain unchanged (Grosshans & Papalexandris 2017a). In particle-particle collisions, the velocity vectors are updated according to Hertzian theory, where we consider monodispersed particles $r_{ij} = r_{ji}$.

The force due to gravitational acceleration \mathbf{g} is based on the density ratio of the fluid to the particle and reads as $\mathbf{f}_g = (1 - (\rho/\rho_p)) \mathbf{g}$.

The electrostatic force is considered with a hybrid scheme which combines Gauss' and Coulomb's law (Grosshans & Papalexandris 2017c). Coulomb law is assumed to have no numerical inaccuracy, as it is mesh independent; however, the computational effort scales with the number of particles $N(N - 1)/2 \sim O(N^2)$, as the force has to be computed for every particle pair. The numerical accuracy of Gauss law strongly depends on the mesh resolution, but only depends linearly on the number of particles N . Hence, the hybrid approach combines the advantages of both methods by considering Coulomb law for nearby particles (within the same cell) and the effect of all other particles in the far field by Gauss law. The force based on Coulomb law for particle ij can be described as

$$\mathbf{f}_{el,Coulomb,ij} = \frac{q_{ij} q_{ji}}{4\pi\epsilon} \frac{\hat{\mathbf{s}}_{12}}{|\mathbf{s}_{ij} - \mathbf{s}_{ji}|^2} \quad (2.10)$$

where \mathbf{s} describes the location of the particle centre, $\hat{\mathbf{s}}_{12}$ a unit vector from particle ij to ji , q the electric charge of the individual particles, and ϵ the electric permittivity of air, which is assumed to be equal to the permittivity of the vacuum, ϵ_0 . The force for the other particle is, according to Newton's third law, $\mathbf{f}_{el,Coulomb,ji} = -\mathbf{f}_{el,Coulomb,ij}$. The calculation

via Gauss's law utilised the electric field created by the charged particles:

$$\mathbf{f}_{\text{el,Gauss}} = \frac{q\mathbf{E}}{m_p} \quad (2.11)$$

with the particle mass m_p , in case of spherical particles $m_p = \frac{1}{6}\pi d_p^3 \rho_p$. The electric field strength, \mathbf{E} , equals the negative gradient of the electric potential, ϕ , i.e., $\mathbf{E} = -\nabla\phi$.

The relation between the electric potential and the electric charge density ρ_{el} is given by the Poisson equation $\nabla^2\phi = -(\rho_{\text{el}}/\epsilon)$. The integration of ρ_{el} over a control volume \mathcal{V} , which contains n particles, is equivalent to the sum of the charges of the n particles. In this case, the control volume \mathcal{V} is represented by a grid cell.

In the following, various levels of coupling between the fluid and particle phases are considered. In 1-way coupling, particle motion is influenced solely by the aerodynamic force, \mathbf{f}_{ad} , and the gravitational force, \mathbf{f}_g . In 2-way coupling, the particle momentum is fed back to the fluid through the term \mathbf{F}_s in equation 2.1b. In 4-way coupling, particles also interact with one another via the particle-particle collision force, \mathbf{f}_{coll} , in equation (2.7), as well as through the electric force term, \mathbf{f}_{el} , in equation (2.7).

2.3. Charging models

The effect of triboelectric charging has been implemented in various models. We have implemented in triboFoam the conventional condenser model (Soo 1971), a simple random charging model (Ozler & Grosshans 2025), a model which transfers a constant charge, and the recently published Stochastic Scaling Model (SSM) (Grosshans *et al.* 2025).

2.3.1. Condenser model

The condenser model computes the charge transfer in a particle-particle collision by

$$\Delta q_{ij} = -\Delta q_{ji} = \frac{C_{ij}C_{ji}}{C_{ij} + C_{ji}} \left(\frac{q_{ji}}{C_{ji}} - \frac{q_{ij}}{C_{ij}} \right) \left(1 - e^{-\Delta t_{12}/T_{12}} \right), \quad (2.12)$$

where Δt_{12} is the contact time during particle-particle collision, T_{12} is the charge relaxation time, and C_{ij} respectively C_{ji} are the electric capacities of both particles. The electric capacity of particle ij is computed as $C_{ij} = 4\pi\epsilon d_{ij}/2$ while C_{ji} is determined accordingly. Further, the charge relaxation time T_{12} is expressed by

$$T_{12} = \frac{C_{ij}C_{ji}}{C_{ij} + C_{ji}} \frac{d_{ij} + d_{ji}}{2A_{12}} \varphi_p, \quad (2.13)$$

where the resistivity of the particle is denoted by φ_p . The calculation of the contact surface A_{12} is performed in accordance with the elastic theory of Hertz as

$$A_{12} = \frac{\pi d_{ij} d_{ji}}{2(d_{ij} + d_{ji})} \alpha_{12} \quad (2.14)$$

with

$$\alpha_{12} = \frac{d_{ij} d_{ji}}{2} \left(\frac{5}{8} \pi \rho_p (1 + k_e) |\mathbf{u}_{12}|^2 \frac{\sqrt{d_{ij} + d_{ji}}}{d_{ij}^3 + d_{ji}^3} \frac{1 - \mu_p}{E_p} \right)^{2/5}. \quad (2.15)$$

In this expression, \mathbf{u}_{12} denotes the relative velocity between the two colliding particles, defined as $\mathbf{u}_{12} = \mathbf{u}_{ji} - \mathbf{u}_{ij}$. The parameters μ_p and E_p represent, respectively, the Poisson ratio and Young's modulus of the particle material. The contact duration, Δt_{12} , is obtained from Hertzian contact theory as $\Delta t_{12} = (2.94\alpha_{12}) / (|\mathbf{u}_{12}|)$.

The computation of charge transfer during particle–wall collisions follows the model proposed by John *et al.* (1980), obtained from the particle–particle charge exchange formulation of Soo (1971), in the limit where the diameter of one particle tends to infinity. The total charge exchange, Δq_w , is expressed as the sum of two distinct contributions,

$$\Delta q_w = \Delta q_c + \Delta q_t. \quad (2.16)$$

Here, Δq_c denotes the dynamic charge transfer due to the contact potential and Δq_t the transfer of the particle’s pre-existing charge. The contact area between the particle and the channel wall is assumed to be small compared to the particle surface area. Consequently, the dynamic charge transfer is modelled analogously to the charging of a parallel-plate capacitor. In this framework, the particle–wall charge exchange, Δq_c , is

$$\Delta q_c = -CU_c \left(1 - e^{-\Delta t_w/T_w}\right) \quad (2.17)$$

where C is the electrical capacitance, U_c is the particle–wall contact potential, Δt_w is the duration of the particle–wall collision, and T_w is the charge relaxation time. The capacitance of a parallel-plate capacitor is given by

$$C = \frac{\epsilon A_{iw}}{h} \quad (2.18)$$

where h denotes the separation between the capacitor plates and A_{iw} is the plate area. In the present context, h corresponds to the effective particle–wall separation during impact, while A_{iw} represents the contact area between the particle and the wall. The latter is estimated from Hertzian elastic theory (see John *et al.* (1980)) by

$$A_{iw} = \pi \frac{d_p}{2} \alpha_{iw} \quad (2.19)$$

with

$$\alpha_{iw} = \frac{d_p}{2} \left(\frac{5}{8} \pi \rho_p (1 + k_e) |\mathbf{u}_i|^2 \left(\frac{1 - \mu_p^2}{E_p} + \frac{1 - \mu_w^2}{E_w} \right) \right)^{2/5}. \quad (2.20)$$

The parameters μ_w and E_w represent the Poisson ratio and Young’s modulus, respectively, of the wall material. Following the arguments of John *et al.* (1980), the plate separation distance h in equation (2.18) is taken to be of the order of the range of repulsive molecular forces arising from surface irregularities. Hertzian contact theory is also applied to estimate the collision duration Δt_w appearing in equation (2.17). According to this theory, Δt_w is given by

$$\Delta t_w = \frac{2.94}{|\mathbf{u}_i|} \alpha_{iw}. \quad (2.21)$$

Furthermore, the charge relaxation time T_w appearing in equation (2.17) is determined by $T_w = \epsilon_w \epsilon_0 \varphi_p$. In this expression, ϵ_w denotes the relative permittivity of the plates, and φ_p is the electrical resistivity of the particle.

The particle pre-charge, q , refers to the charge present prior to its collision with the wall, and is assumed to be uniformly distributed over its surface. The corresponding pre-charge transfer across the contact surface, Δq_t , is therefore given by

$$\Delta q_t = -\frac{1}{4} \alpha_{iw} q. \quad (2.22)$$

The assumption of a uniformly distributed pre-charge does not generally hold for non-conducting particle surfaces (Grosshans & Papalexandris 2017b). For the cases considered

in the present study, however, the charge accumulated by each particle remains much smaller than its equilibrium value. As a result, the contribution of Δq_t to the total charge transfer is negligible compared with that of Δq_c , and the use of equation (2.22) is sufficiently accurate for the purposes of the present analysis.

2.3.2. Stochastic scaling model

Contrary to the condenser model, the new SSM (Grosshans *et al.* 2025) can predict three experimentally observed charging patterns: (a) scattered particle-wall impact charge (Grosjean & Waitukaitis 2023b), (b) size-dependent particle-particle (bipolar) charging (Forward *et al.* 2009), and (c) charge reversal after some wall impacts (Shaw & Jex 1928). The SSM unifies the charging of particles of the same material (particle-particle) and of different materials (particle-wall) in a single framework. This framework is based on a stochastic closure involving the mean, variance, skewness, and minimum impact charge obtained from a single reference experiment.

Similar to the mosaic (Apodaca *et al.* 2019; Grosjean & Waitukaitis 2023a) and surface state models (Lowell & Truscott 1986a,b; Lacks *et al.* 2008; Lacks & Levandovsky 2007), the contact area between the particle and another surface consists of charge-exchange sites. When particles collide with a wall, each of the N_w active charging sites on the wall contributes a charge ϵ_w to the particle. Hence, the total transfer from the wall to the particle equals to $\Delta q_w = \epsilon_w N_w \sim F(\mu_w)$, where μ_w corresponds to the expected value of Δq_w . In the case of a conductive and grounded wall, the charging sites regenerate immediately upon contact. This maintains a consistent number of active sites both before and after impact.

On the other hand, according to SSM, charge transfer from an insulative particle surface is probabilistic. Each of the N_{ij} active charging sites that make up the contact area of particle ij can either transfer a charge ϵ_{ij} to the opposing surface or not. This stochastic process follows a binomial distribution, which is approximated by a skewed normal distribution characterised by a mean μ_{ij} , a standard deviation σ_{ij} and a skewness γ_{ij} and can be expressed as

$$\Delta q_1 = \epsilon_p \sum_{n=1}^{N_{ij}} \theta_n \sim G(\mu_{ij}, \sigma_{ij}, \gamma_{ij}), \quad (2.23)$$

with the Bernoulli random variable θ_n of equal probability of 0 or 1.

To obtain the charge transfer during an individual collision, the statistical parameters μ_w , μ_{ij} , σ_{ij} , and γ_{ij} are scaled from a reference experiment with known parameters μ_0 , σ_0 , γ_0 , N_{w0} , and N_0 to the actual number of active charging sites N_w and N_{ij} by the relations

$$\mu_w = \Delta q_{0,\min} \frac{N_w}{N_{w0}} \quad (2.24a)$$

$$\mu_i = (\Delta q_{0,\min} - \mu_0) \frac{N_i}{N_0} \quad (2.24b)$$

$$\sigma_i = \sigma_0 \sqrt{\frac{N_i}{N_0}} \quad (2.24c)$$

$$\gamma_i = -\gamma_0 \frac{N_0}{N_i} \quad (2.24d)$$

with

$$\frac{N_w}{N_{w0}} = \frac{A}{A_0} \frac{\chi}{\chi_0} \quad \text{and} \quad \frac{N_i}{N_0} = \frac{A}{A_0} \frac{\chi}{\chi_0} \frac{c}{c_0}. \quad (2.24e)$$

The contact area A is estimated from Hertzian contact theory as described above.

The activity ratio χ/χ_0 , the ratio of active to total charging sites, is obtained from

$$\frac{\chi}{\chi_0} = \frac{\chi_w}{\chi_0} = 1 - \text{sgn}(\Delta q_{0,\min}) \frac{4q_i}{C_{\text{sat}} d_i^2} \quad (2.25a)$$

$$\frac{\chi}{\chi_0} = \frac{\chi_i}{\chi_0} = 1 + \text{sgn}(\Delta q_{0,\min} - \mu_0) \frac{4q_i}{C_{\text{sat}} d_i^2} \quad (2.25b)$$

$$\frac{\chi}{\chi_0} = \frac{\chi_{ij}}{\chi_0} = 1 - \text{sgn}(\Delta q_{0,\min} - \mu_0) \frac{8}{C_{\text{sat}}} \left(\frac{q_j}{d_j^2} - \frac{q_i}{d_i^2} \right) \quad (2.25c)$$

with $0 \leq \chi/\chi_0 \leq 1$, where C_{sat} denotes a fitting parameter. Numerical simulations for air at atmospheric pressure and unit permittivity yielded $C_{\text{sat}} = 500 \mu\text{C m}^{-2}$ (Matsuyama *et al.* 2003).

The charging site density c/c_0 ($0 \leq c/c_0 \leq 1$) is a function of the number of collisions M and is computed for the m th contact as

$$\frac{c}{c_0} (t_{M-1} \leq t \leq t_M) = 1 - \sum_{m=1}^{M-1} \frac{c_{m-1}}{c_0} \frac{A_m}{A_p} \frac{\chi_m}{\chi_0} \frac{q_{i,m}}{q_{i,\max}} \quad (2.26)$$

where A_m/A_p is the ratio of the contact area to the particle surface area.

The reference experiment for determining the parameters with the subscript 0 consists of the normal impact of a single particle onto a fixed plate. Particles of diameter d_0 are released onto the target, and the wall-normal impact velocity $u_{n,0}$ is obtained from high-speed imaging. The associated charge transfer is quantified following the procedure of Matsuyama *et al.* (2003). Repeated realisations of the experiment yield statistical distributions from which μ_0 , σ_0 , γ_0 , and $\Delta q_{0,\min}$ are evaluated. Further details of the model formulation and experimental configuration are provided by Grosshans *et al.* (2025).

3. Numerical setup

Two different numerical setups are utilised in this work. The first validates the triboFoam solver using DNS. The second uses LES to study the effects of higher Reynolds numbers on particle mechanics and charging. The subsequent sections describe both setups.

3.1. DNS setup for the validation of triboFoam

The solver triboFoam is validated against pafiX, because, to the best of our knowledge, pafiX is the only existing open-source solver for triboelectric particle charging. The motion of the fluid and uncharged particles has been validated against literature data (Sardina *et al.* 2012; Vreman & Kuerten 2014). Since pafiX is a DNS solver and to avoid interference with a turbulence model, triboFoam validation is based on DNS of turbulent channel flows, first for uncharged and then for charged particles.

The channel flows are fully-developed at a fixed friction Reynolds number of $Re_\tau = u_\tau \delta / \nu = 180$ with the friction velocity $u_\tau = \sqrt{\tau_w / \rho}$, where τ_w is the wall shear stress, and the half channel height δ . In the following, quantities indicated with the superscript $+$ are dimensionless with u_τ to obtain values in wall units. Hence, the streamwise velocity u^+ is defined as $u^+ = u/u_\tau$, the wall-normal distance as $y^+ = (yu_\tau) / \nu$, and the time as $t^+ = (tu_\tau^2) / \nu$.

The size of the computational domain is $12\delta \times 2\delta \times 4\delta$ in streamwise (x), wall-normal (y), and spanwise (z) direction with $\delta = 0.02$ m. In streamwise and spanwise directions,

Parameter	Symbol	Value
Poisson's ratio, particle	μ_p	0.4
Young's modulus, particle	E_p	$10^8 \text{ kg s}^{-2} \text{ m}^{-1}$
Resistivity, particle	φ_p	$10^{13} \Omega \text{ m}$
Particle restitution ratio	k_e	0.95
Poisson's ratio, wall	μ_w	0.28
Young's modulus, wall	E_w	$10^{11} \text{ kg s}^{-2} \text{ m}^{-1}$
Relative permittivity, wall	ε_w	5.0
Effective separation	h	10^{-9} m
Air permittivity	ε	$8.854 \cdot 10^{-12} \text{ F m}^{-1}$
Air kinematic viscosity	ν	$1.46 \cdot 10^{-5} \text{ m}^2 \text{ s}^{-1}$
Air density	ρ	1.2 kg m^{-3}
Particle density	ρ_p	1150 kg m^{-3}

Table 1. Material properties for the simulations (Grosshans & Papalexandris 2017a).

periodic boundary conditions are applied, while the wall features the no-slip condition. The fluid is driven by a constant pressure gradient, and its properties are set to be equivalent to those of air. The numerical values of all material parameters in the simulations are summarised in table 1. The spatial resolution in stream- and spanwise direction amounts to $\Delta x^+ \approx 8.44$ and $\Delta z^+ \approx 5$, respectively. In wall-normal direction, the size of the first cell at the wall equals $\Delta y^+ \approx 0.036$ and in the channel centre $\Delta y^+ \approx 4$. All derivatives of the Navier-Stokes and the electrostatic equations are discretised second order in time and space using finite volumes.

Three different particle sizes were investigated, $d_p = 25 \mu\text{m}, 50 \mu\text{m}, 100 \mu\text{m}$ while keeping the material density (table 1) and the particle number density ($C = 10^8 \text{ m}^{-3}$) constant. In this case, the gravity vector is set to zero. This setup was chosen as it represents realistic conditions even though the particle volume fraction ω rises with increasing d_p . The values set for the particles correspond to the material polymethylmethacrylate (PMMA), which is a typical plastic transported by pneumatic conveying.

The Stokes number, St , is defined as the ratio between particle response time, $T_r = \frac{1}{18} \rho_p d_p^2 \rho^{-1} \nu^{-1}$, and a characteristic time scale of the fluid flow, $T_f = \delta u_c^{-1}$, with the centreline velocity u_c , resulting in

$$St = \frac{1}{18} \frac{\rho_p}{\rho} \frac{d_p^2}{\nu} \frac{u_c}{\delta}. \quad (3.1)$$

Due to different particle sizes, the Stokes number differs per simulation. For Stokes numbers much greater than unity, particle trajectories are only weakly influenced by the surrounding flow. Conversely, when the Stokes number is much less than unity, particle motion closely follows the pathlines of the flow. The Stokes numbers and other dimensional quantities for the different particle sizes are given in table 2.

The simulations on particle charging start with a fully-developed fluid and particle flow field as initial condition. The particles have an initial charge of $q = 0$. In the case of the condenser model, a saturation charge of $q_{\text{sat}} = 1.26^{-13} \text{ C}$ is set which corresponds to about 10 % of the maximum charge a $d_p = 50 \mu\text{m}$ particle can hold (Matsuyama 2018). For the SSM, the reference parameters are chosen as $r_0 = 2 \cdot 10^{-4} \text{ m}$, $u_{n,0} = 0.925 \text{ m s}^{-1}$, $\mu_0 = -4.12 \cdot 10^{-15} \text{ C}$, $\sigma_0 = 6.49 \cdot 10^{-15} \text{ C}$, $\gamma_0 = -0.191$, and $\Delta q_{0,\text{min}} = -2.19 \cdot 10^{-14} \text{ C}$ (Grosshans *et al.* 2025). Inherently, the SSM considers a size-dependent saturation charge due to its formulation. For the chosen reference experiment parameters, a $d_p = 25 \mu\text{m}$

	Re_τ	$d_p/\mu\text{m}$	d_p^+	$u_c/(\text{m/s})$	St	ω
DNS	180	25	0.22	2.50	0.28	0.82
	180	50	0.45	2.50	1.14	6.54
	180	100	0.90	2.50	4.56	52.36
LES	180	25	0.22	2.38	0.27	0.82
	180	50	0.45	2.38	1.08	6.54
	180	100	0.90	2.38	4.34	52.36
	300	25	0.37	4.39	0.50	0.82
	300	50	0.75	4.37	1.99	6.54
	300	100	1.50	4.36	7.95	52.36
	395	25	0.49	5.91	0.67	0.82
	395	50	0.99	5.92	2.70	6.54
	395	100	1.97	5.94	10.83	52.36
	550	25	0.69	8.38	0.95	0.82
	550	50	1.37	8.38	3.82	6.54
	550	100	2.75	8.41	15.33	52.36

Table 2. Overview of the non-dimensional particle parameters for DNS at $Re_\tau = 180$ and LES from $Re_\tau = 180$ to $Re_\tau = 550$

particle reaches a saturation charge of about $7.81 \cdot 10^{-15} \text{ C}$, a $d_p = 50 \mu\text{m}$ particle $3.13 \cdot 10^{-13} \text{ C}$, and a $d_p = 100 \mu\text{m}$ particle $1.25 \cdot 10^{-12} \text{ C}$.

The simulations presented after the validation of the SSM employ the condenser model. Owing to its fully deterministic formulation, this model allows for a clear attribution of the observed charging behaviour to the underlying physical mechanisms and thus facilitates a deeper understanding of the factors contributing to particle charging. One of the defining features of the SSM is its ability to account for variable impact charging. Nevertheless, the SSM can be rendered fully deterministic by setting $\sigma_0 = \gamma_0 = 0$. Under this restriction, charging behaviour closely resembling that of the condenser model can be recovered by choosing $\mu_0 = \Delta q_{0,\min} = \mu_{\text{condenser}}$. The parameter $\mu_{\text{condenser}}$ depends on the wall-normal impact velocity u_n and the particle diameter d_p . Here, $u_n = 0.01 \text{ m s}^{-1}$ is selected to match the average wall-normal particle impact velocity observed in the simulations. For this configuration, particles with diameters $d_p = 25 \mu\text{m}$ require $\mu_{\text{condenser}} = 2.77 \cdot 10^{-10} \text{ C}$, particles with $d_p = 50 \mu\text{m}$ require $\mu_{\text{condenser}} = 2.14 \cdot 10^{-13} \text{ C}$, and particles with $d_p = 100 \mu\text{m}$ require $\mu_{\text{condenser}} = 7.71 \cdot 10^{-15} \text{ C}$.

Section D shows the evolution of the particle charge as a function of the number of impacts for this parameter constellation. The results indicate that the charging behaviour predicted by the two models is nearly identical up to approximately 10^4 collisions. Since such a high number of impacts is never attained in the simulations considered here, the condenser model and the deterministic limit of the SSM can be regarded as equivalent under the present conditions.

3.2. LES setup for varying Reynolds numbers

For the LES presented herein, we established the computational grid through a grid-sensitivity study in which the predicted velocity field and particle distribution were compared to results from DNS. A detailed description of this procedure is provided in Section A. The study indicated that streamwise and spanwise resolutions of $\Delta x^+ \approx 9.88$ and $\Delta z^+ \approx 6.58$, respectively, are sufficient. In the wall-normal direction, the first cell adjacent to the wall has a size of $\Delta y_w^+ \approx 0.47$, while at the channel centre the spacing

is $\Delta y_c^+ \approx 6.25$. This resolution is adequate for all friction Reynolds numbers considered, up to $Re_\tau = 550$. Moreover, it was observed that with increasing Re_τ , the grid resolution in wall units could be further reduced without loss of accuracy, especially in streamwise direction. Hence, simulations at $Re_\tau = 550$ were conducted with a streamwise resolution of $\Delta x^+ \approx 19.75$.

4. Presentation and discussion of the numerical results

In this section the obtained results are presented and discussed starting with the validation of the triboFoam solver using 1-way coupling. In the next step, the effect of 4-way coupling is assessed, followed by the validation of the LES setup by a comparison to DNS data at $Re_\tau = 180$. Finally, the effect of increasing Reynolds number on triboelectric charging is evaluated.

4.1. Validation of *triboFoam*

The first step of the validation considers a fully developed flow of uncharged particles which are 1-way coupled to the flow, considering only the drag force, f_d . Figure 1a depicts the mean velocity profile of the streamwise component over the wall-normal coordinate for triboFoam and pafiX, each with three different particle sizes. The profiles show the typical shape of the universal law of the wall consisting of the viscous sublayer, buffer layer, and logarithmic domain. The comparison to the data of Lee & Moser (2015) reveals a maximum deviation of less than 1 %. The different particle sizes have no impact on the profile as the simulations feature only 1-way coupling.

Figure 1b shows the relative particle concentration, \bar{C}_{rel} , as a function of wall-normal distance. The relative concentration is defined as

$$\bar{C}_{\text{rel}} = \frac{\bar{C}}{C_0}, \quad (4.1)$$

where \bar{C} denotes the temporally averaged particle concentration at wall-normal location y , and C_0 is the mean particle concentration across the entire channel. The distribution is obtained from a histogram whose bins coincide with the cells of the computational grid, which are identical for both solvers. The results demonstrate close agreement between the two solvers. In all simulations, a particle concentration increases in the near-wall region due to turbophoretic drift (Li *et al.* 2021; Ozler & Grosshans 2025), with a pronounced peak one particle radius from the wall, $y^+ = d_p^+/2$. Consequently, as the particle diameter increases, the peak shifts progressively towards the channel centre. With decreasing particle diameter, the distribution becomes more uniform, which is consistent with the observations of Sardina *et al.* (2012).

In the final step, the charging models are validated by comparing the temporal evolution of the particle charge. To this end, the average charge across all particles, $\langle q \rangle$, is normalised by the saturation charge, q_{sat} , to obtain the relative charge $\langle q \rangle_{\text{rel}} = \langle q \rangle / q_{\text{sat}}$. Figure 2 compares the charge build-up for (a) the condenser model and (b) the stochastic scaling model across both solvers for all three particle sizes. Both charging models and both solvers exhibit the same overall physical trend: within the investigated diameter range, larger particles charge more rapidly than smaller ones. This is attributed to two effects. First, larger particles experience higher collision velocities, which, according to Hertzian contact theory, lead to larger contact areas and thus greater charge transfer per collision (see equations (2.19) and (2.20)). Second, the collision frequency increases when the particle diameter rises from $d_p = 25 \mu\text{m}$ to $50 \mu\text{m}$. Increasing the size further to $d_p = 100 \mu\text{m}$ results in a

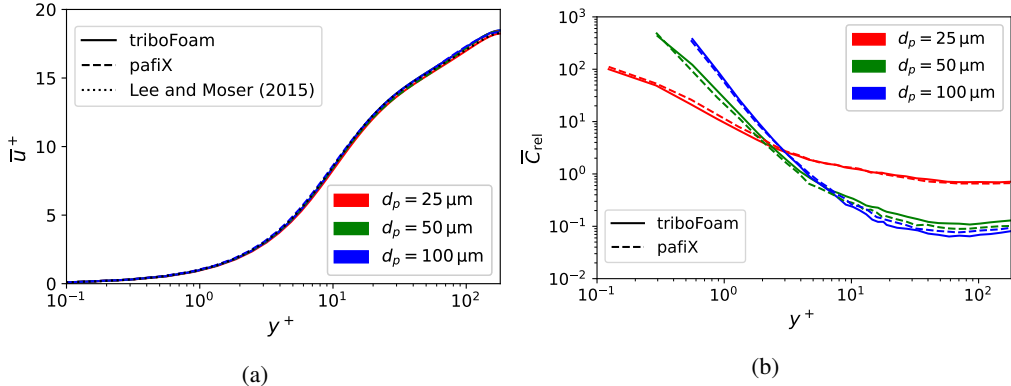


Figure 1. (a) Velocity \bar{u}^+ and (b) relative particle density \bar{C}_{rel} plotted over wall-normal distance y^+ for triboFoam (solid) and pafiX (dashed) comparing different particle sizes for DNS of $Re_\tau = 180$. The particles are 1-way coupled to the fluid. The concentration of the particles is calculated based on the particle centre.

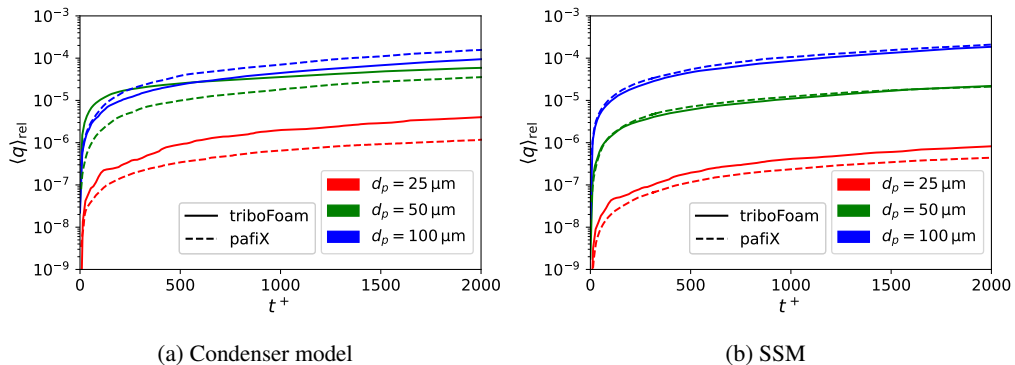


Figure 2. Averaged relative particle charge $\langle q \rangle_{\text{rel}}$ over time for both solvers and different particle sizes for DNS of $Re_\tau = 180$ using (a) the condenser model and (b) the SSM. The particles are 1-way coupled to the fluid.

slightly reduced collision frequency, which is consistent with the lower near-wall particle concentration observed in figure 1b.

Although the qualitative behaviour is consistent between the solvers, quantitative differences remain. For $d_p = 25$ and $d_p = 50 \mu\text{m}$, triboFoam predicts a faster charging rate than pafiX, whereas the opposite behaviour is observed for $100 \mu\text{m}$. The collision frequency and impact velocity depend on the numerical time-step and grid resolution, and this dependency is stronger for pafiX. Therefore, an adequately fine resolution in both space and time was selected and kept constant for all simulations to ensure a consistent basis for comparison ($\Delta t^+ \approx 0.11$). The discrepancies between the solvers are smaller for the SSM than for the condenser model. This is explained by the weaker dependence of the SSM on the contact area, meaning that differences in impact velocity play a smaller role. In addition, fluctuations in the charge build-up become more pronounced with decreasing particle size, particularly in triboFoam. Due to the smaller Stokes number, the motion of these particles is stronger affected by the turbulent fluctuations of the carrier phase, which leads to a more intermittent collision behaviour and hence a more irregular charging process.

The charge build up in the simulation of $25 \mu\text{m}$ particles using the condenser model shows at the beginning a relatively high charging rate, which can be attributed to a turbulent

sweep pushing many particles towards the wall. Afterwards, the charging rate decreases to a comparable level of pafiX and fits also into the progression of the other two triboFoam simulations (see also figure 4). Overall, the comparison demonstrates that the triboFoam charging predictions agree well to those of pafiX, while triboFoam is less sensitive to time-step size and grid resolution, indicating a more robust numerical behaviour. As discussed in the introduction, controlled experimental data for particle charging in fully-developed turbulent flow is unavailable due to the impossibility to control the electrical boundary conditions.

In summary, the turbulent fluid flow, distributions of uncharged particles, and particle charge build-up using the condenser model and SSM simulated with triboFoam has been validated successfully with pafiX and experimental data from the literature.

4.2. Effect of 2-way and 4-way coupling

Up to this point, only 1-way coupling has been considered. In the following, the effects of 2-way and 4-way coupling are examined. Figure 3 shows the wall-normal particle concentration profiles for different particle sizes. Comparing 1-way and 2-way coupling reveals that the particle concentration at the location closest to the wall ($y^+ \approx d_p^+/2$) decreases for particles with a Stokes number greater than 1 when 2-way coupling is included. At larger distances from the wall, however, the concentration increases. This effect is most pronounced for the largest particles. Incorporating 4-way coupling further reduces the near-wall concentration, as particle–particle interactions push particles away from the wall. This reduction is strongest for the largest particles, which occupy the highest volume fraction. Accordingly, the differences between 4-way and 2-way coupling are most significant for the largest particles, owing to the higher frequency of particle–particle collisions at increased volume concentration. These observations are consistent with those of Rupp *et al.* (2023).

Moreover, for particles with $St > 1$, the effect of 4-way versus 2-way coupling is stronger than that of 2-way versus 1-way coupling. This is partially in accordance with Rupp *et al.* (2023), who observed for particles with $St = 0.5$ almost no change at $Re_\tau = 300$. The physical reason for the reduction in particle concentration in the near-wall region when changing from 1-way to 2-way coupling is attributed to turbophoresis. Particles concentrate in regions of low vorticity at the wall. 2-way coupling reduces these concentration peaks as particles diffuse momentum from the bulk towards the wall region. Particle-particle collisions in 4-way coupling even further reduces the near-wall concentration as particles push each other away from the wall.

Figure 4a shows the temporal evolution of the relative mean charge $\langle q \rangle_{\text{rel}}$ as a function of t^+ , while figure 4b presents the corresponding charging rate $\langle q \rangle_{\text{rel}}/dt^+$. Overall, the charging behaviour is dominated by particle size rather than by the coupling mechanism. For particles of $d_p = 25$ and $50 \mu\text{m}$, only minor differences arise between 1-way, 2-way, and 4-way coupling. Specifically, $25 \mu\text{m}$ particles exhibit a slightly faster charge build-up when switching from 1-way to 2-way coupling, whereas 4-way coupling causes almost no additional change. For particles of $d_p = 50 \mu\text{m}$, the opposite trend is observed: the transition from 1-way to 2-way coupling barely affects the charging dynamics, while 4-way coupling yields a modest increase in charging rate. In contrast, $100 \mu\text{m}$ particles experience a more notable enhancement in charging rate when switching from 1-way to 2-way coupling (by approximately 22 %), followed by an even stronger increase of about 296 % when activating 4-way coupling, as illustrated in figure 4b.

Figure 4 shows a longer time interval up to $t^+ = 15\,000$ than figure 2a, although the system is still in the early charging stage with the average charge remaining below 1 % of q_{sat} . The focus of this work is placed on this early phase of charging, when the most

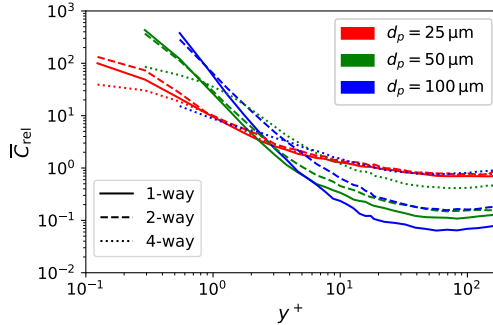


Figure 3. Relative particle density \bar{C}_{rel} plotted over wall-normal coordinate y^+ for uncharged particles of different sizes for DNS of $Re_\tau = 180$. The coupling between the particles and the fluid is varied between 1-way, 2-way, and 4-way. The particle concentration profiles are based on the particle centre.

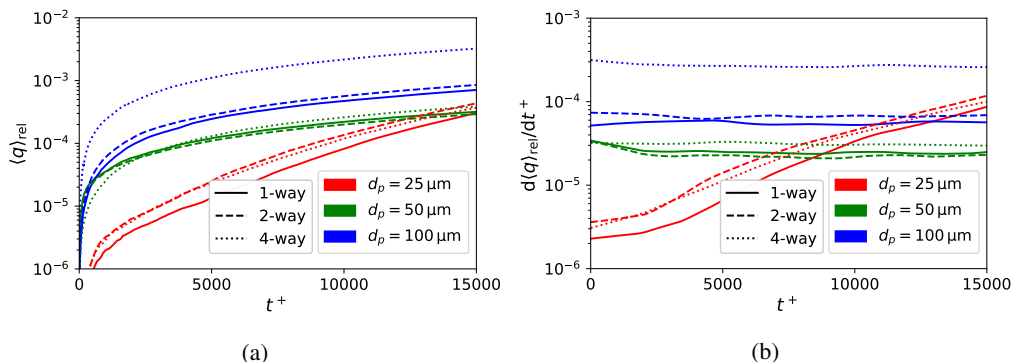


Figure 4. (a) Average relative particle charge $\langle q \rangle_{\text{rel}}$ and (b) charging rate $\langle q \rangle_{\text{rel}}/dt^+$ over time for different particle sizes and particle-fluid coupling complexities for DNS of $Re_\tau = 180$.

significant differences between configurations occur, whereas the charging rates decay once saturation charge is approached (Ozler & Grosshans 2025). Within this investigated time, no significant temporal variation in the charging rate is observed for particles of $d_p = 50 \mu\text{m}$ and $100 \mu\text{m}$. However, $d_p = 25 \mu\text{m}$ particles exhibit an almost logarithmic increase in charging rate that gradually weakens as saturation becomes imminent. As a consequence, these small particles eventually surpass the charging rate of particles with $d_p = 50 \mu\text{m}$ for $t^+ \gtrsim 8000$ and even exceed the rate of $100 \mu\text{m}$ particles under 1-way and 2-way coupling once $t^+ \gtrsim 13000$. This behaviour originates from electrostatic forces—without them, the effect does not occur (not shown here).

To gain further insight into the charging rates and their underlying physical mechanisms, the two principal drivers of charge transfer are shown in figure 5: (a) the temporal evolution of the collision rate and (b) the collision velocity distribution of uncharged particles. The time history of the collision rate exhibits a qualitative resemblance to the charging rate, indicating that the observed behaviour is primarily governed by the collision frequency. Particles of $d_p = 50 \mu\text{m}$ and $100 \mu\text{m}$ experience an almost constant collision rate throughout the analysed period, whereas particles of $d_p = 25 \mu\text{m}$ show an increase by roughly one order of magnitude within the same interval.

For particles with $St > 1$, the collision rate decreases from 1-way to 2-way and onwards to 4-way coupling, which is consistent with the reduction of particle concentration in the very near-wall region shown in figure 3. In contrast, particles of $d_p = 25 \mu\text{m}$ experience

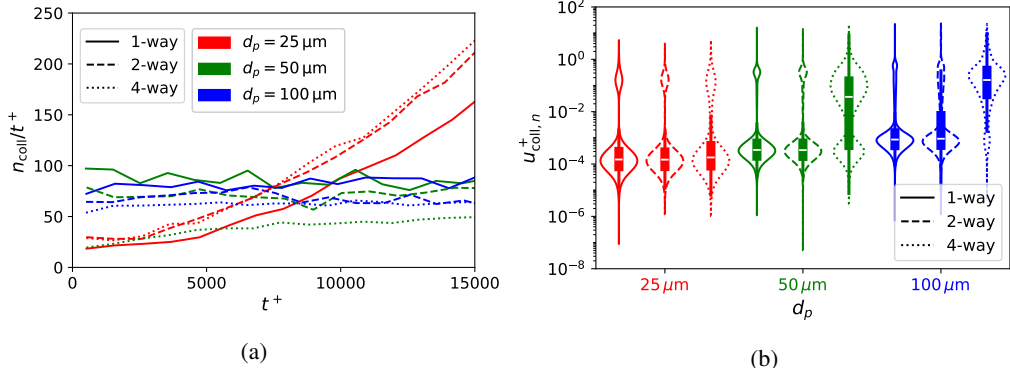


Figure 5. (a) Particle-wall collision rates n_{coll}/t^+ and (b) distributions of the wall-normal collision velocity $u_{\text{coll},n}^+$ over time for different particle sizes and coupling complexities for DNS of $Re_\tau = 180$.

an increase in collision frequency when switching from 1-way to 2-way coupling, again in agreement with the corresponding concentration distribution. Interestingly, although 4-way coupling reduces the near-wall concentration for these small particles, the collision rate remains nearly unchanged relative to the 2-way case. This suggests that particle-particle reflections in the near-wall region compensate for the reduced particle density by redirecting off-bouncing particles back toward the wall, thereby maintaining the collision frequency.

The rise in collision rate for the $d_p = 25 \mu\text{m}$ particles is an electrostatic effect. Larger particles do not show this behaviour, as their electric Stokes number is too small for electrostatic forces to exert a notable influence on their dynamics. The increased collision frequency is therefore attributable exclusively to charged particles, which exhibit a heightened probability of rebounding collisions. Two electrostatic mechanisms are possible: repulsion from already charged particles in the channel core, and attraction toward the wall, which—as a grounded conductor—maintains zero electric potential. The latter mechanism is dominant, as simulations employing only Coulomb forces between particles do not reproduce the increased collision rate; only the Gauss-law component of the hybrid charging model produces such behaviour. It describes the effect of an image charge generated in the conductive wall which attracts the particles to the wall (Ozler & Grosshans 2025).

Since the time evolution of particle charging rate and particle-wall collision frequency match almost perfectly for $d_p = 25 \mu\text{m}$, the coupling mechanism has no significant influence on the collision, as confirmed by figure 5b. The collision-velocity distribution, shown for uncharged particles averaged over the charging period, exhibits no significant temporal variation. Overall, the distribution is bimodal: the lower mode corresponds to particles grazing the wall with small tangential contact velocities, whereas the higher mode arises from particles impinging during sweeps originating from the channel centre.

For $d_p = 25 \mu\text{m}$, the collision-velocity distributions for 1-way and 2-way coupling are nearly identical, as the particle inertia is too small to transport substantial momentum from the bulk toward the wall. When 4-way coupling is enabled, the number of high-speed impacts and the distribution's overall spread slightly increases. This increase is due to particle-particle collisions in the near-wall region that redirect previously rebounding particles back toward the wall. For $d_p = 50 \mu\text{m}$, the transition from 1-way to 2-way coupling again produces only minor changes. However, under 4-way coupling the collision rate decreases while the charging rate increases markedly. This increase is linked to a rise

of the average collision velocity by about two orders of magnitude. The corresponding distribution demonstrates a shift in the dominant collision mechanism, with high-speed impacts overtaking the low-speed grazing events.

For the largest particles, $d_p = 100 \mu\text{m}$, the same qualitative trends are observed, but now even 2-way coupling produces noticeable changes, as the particle inertia becomes sufficient to transport significant momentum toward the channel wall. Under 4-way coupling, the low-speed grazing events nearly vanish, consistent with the reduction in particle concentration at $y^+ \approx d_p^+/2$ in figure 3. The increased diameter raises the likelihood that near-wall particles are displaced by particles arriving from the channel core, and this effect becomes so dominant that the reduced collision frequency is fully outweighed by the substantially higher charge transfer per collision, leading to an overall increase in the charging rate of the particle ensemble.

4.3. Extension toward LES

This section validates the LES model at a friction Reynolds number of $Re_\tau = 180$ as a preparation for the subsequent analysis at higher Reynolds numbers. In a precursor study, we determined an appropriate grid resolution, see Section C. In addition, different subgrid-scale closure models were evaluated, see Section B, where the WALE closure model performed best. In general, provided that the grid resolution is sufficient, LES reproduces the DNS results with good accuracy. Figure 6a compares the wall-normal particle concentration profiles obtained from LES and DNS. The agreement is best for the largest particles and decreases with decreasing Stokes number. In particular, LES underpredicts the near-wall particle concentration, with maximum deviations of approximately 10 % for $d_p = 25 \mu\text{m}$, 5 % for $d_p = 50 \mu\text{m}$, and 1 % for $d_p = 100 \mu\text{m}$. This trend is due to LES not resolving the smallest turbulent scales, and since small particles are most strongly influenced by these flow structures, the reduced representation of near-wall turbulence diminishes turbophoretic transport, leading to lower predicted concentrations at the wall (Kuerten & Vreman 2004).

Figure 6b presents the comparison between DNS and LES with respect to the temporal evolution of the relative particle charge. Overall, the LES reproduces the DNS. During the initial charging phase, the LES predictions for particles of $d_p = 25 \mu\text{m}$ agree well with the DNS. With increasing particle diameter, the LES begins to overpredict the charging, and this deviation grows systematically with particle size. For $t^+ \gtrsim 4000$, the LES results for $d_p = 50 \mu\text{m}$ and $d_p = 100 \mu\text{m}$ continue to exceed the DNS values because the LES charging rate remains approximately constant. The same behaviour is observed for the $d_p = 25 \mu\text{m}$ particles; however, since the DNS exhibits an increase in charging rate in this regime, the LES increasingly underpredicts the DNS for this smallest particle class.

Further insights into these discrepancies are provided by the comparison of particle–wall collision rate and collision velocity shown in figure 7. For the smallest particles of $d_p = 25 \mu\text{m}$, the dominant source of deviation lies in the collision rate. The electrostatic mechanism associated with the grounded wall, arising from the Gauss-law component of the electrostatic model, is significantly weaker in the LES. This behaviour is directly linked to grid resolution: Gauss's law is Eulerian and therefore grid dependent; the coarser LES grid resolves gradients in the electric potential less sharp; weaker potential gradients produce weaker electrostatic forces; and, as a result, particles are more likely to rebound from the wall, re-enter the turbulent flow, and be convectively transported away from the wall. Consequently, the LES underestimates the electrostatically enhanced collision frequency.

For the intermediate particle size, $d_p = 50 \mu\text{m}$, the DNS shows a moderate increase in collision rate over time, and this effect is partly reproduced by the LES. However, an

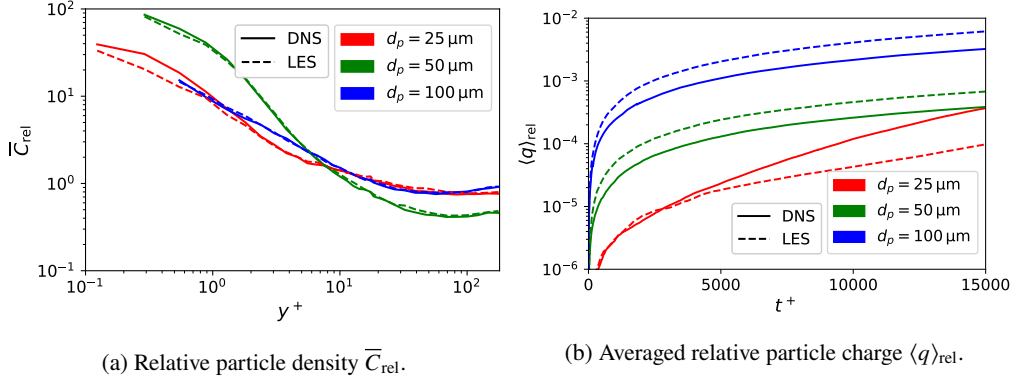


Figure 6. (a) Relative particle density based on the particle center \bar{C}_{rel} over wall-normal coordinate y^+ for uncharged particles of different sizes. (b) Averaged relative particle charge $\langle q \rangle_{\text{rel}}$ over time for different particle sizes and for DNS and LES of $Re_\tau = 180$.

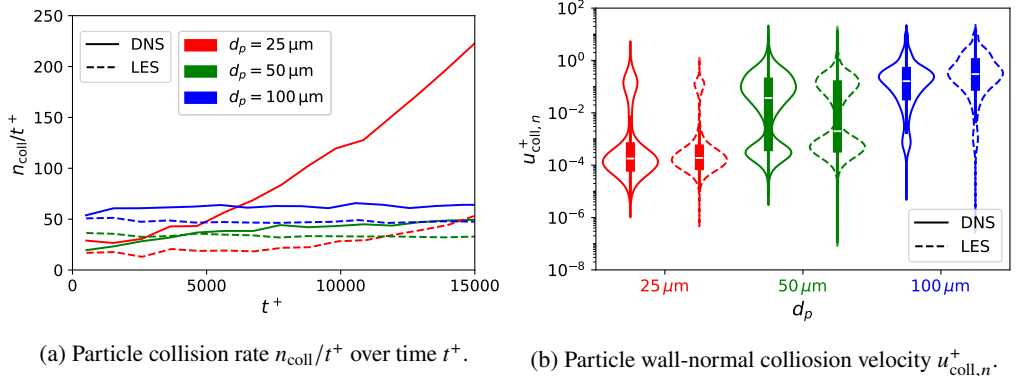


Figure 7. Comparison of (a) particle-wall collision rate n_{coll}/t^+ and (b) distributions of the collision velocity $u_{\text{coll},n}^+$ for different particle sizes and for DNS and LES of $Re_\tau = 180$.

additional mechanism becomes relevant: the LES predicts a higher frequency of high-velocity impacts, which increases the average charge transfer per collision and contributes to the overall overprediction of the charging rate.

For the largest particles of $d_p = 100 \mu\text{m}$, the LES even underpredicts the collision rate relative to the DNS. The resulting overestimation of the charging rate is therefore entirely attributable to an increase in the collision velocity. Both the number of high-speed impacts and the probability of very high impact velocities increase in the LES. These energetic collisions are associated with particles arriving from the channel centre. In the LES, such particles slow less down before hitting the wall. Several mechanisms contribute to this discrepancy. First, LES inherently filters the fluid velocity field, removing small-scale near-wall turbulent structures that in DNS scatter particles and reduce their velocity prior to impact. It has been shown that even well-resolved LES may not accurately reproduce near-wall particle accumulation or preferential segregation due to the absence of these fine scales, leading to errors in particle velocity and concentration statistics near the wall (Marchioli *et al.* 2008). Second, the filtering introduced by LES alters the forces acting on particles, and the associated filtering error is largest in the buffer region where near-wall interactions are most critical; this can result in less attenuation of particle motion

toward the wall (Bianco *et al.* 2012). Finally, differences in resolved turbulence spectra between LES and DNS influence turbophoresis and local particle concentration gradients, further affecting collision statistics (Kuerten 2016). Each of these effects merits further investigation to quantify their relative influence on particle–wall impact velocities and associated charging.

In summary, LES provides an adequate approach for modelling particle charging with substantially reduced computational cost, while capturing the correct qualitative trends. However, LES may overpredict the charging rate for larger particles, which is conservative from a safety perspective. For small particles, the rebounding effect of charged particles is underestimated. Overall, LES model is validated, allowing for the subsequent investigation of higher carrier-flow Reynolds numbers in the next section.

4.4. Effect of Reynolds number

Using the validated LES, we increased the Reynolds number in the 4-way coupled LES to $Re_\tau = 300, 395$, and 550 . Owing to the higher centreline velocity at increasing Re_τ , the Stokes number St also increases (see table 2). In addition, the particle diameter in wall units becomes larger. Both effects imply that the particle dynamics are governed by the larger turbulent scales.

Figure 8a presents the wall-normal particle concentration profiles for the four investigated Reynolds numbers and the three particle sizes, scaled with the outer length scale (channel height h). Overall, the particle distribution is more influenced by the particle diameter than by the Reynolds number. For the smallest particles ($d_p = 25 \mu\text{m}$), an increase in Re_τ results in a higher particle concentration near the wall. This trend appears asymptotic, with the most pronounced rise occurring between $Re_\tau = 180$ and $Re_\tau = 300$, corresponding to an increase of approximately 570 %. In contrast, for the larger particles ($d_p = 50 \mu\text{m}$ and $d_p = 100 \mu\text{m}$), the opposite behaviour is observed: the near-wall particle concentration decreases with increasing Reynolds number. These observations are consistent with the findings of Bernardini (2014), who reported that the particle concentration in the outer layer scales with outer units, particularly for $St = 1$ and $St \geq 500$. In the range of $10 \geq St \geq 100$, no scaling with the outer layer is reported, which is both in agreement with the trends shown in figure 8a.

For the inner layer, Sardina *et al.* (2013) and Bernardini (2014) proposed a scaling with inner units, especially for intermediate Stokes numbers ($10 \lesssim St \lesssim 25$). Following this approach, Bernardini (2014) introduced a particle concentration in wall units, $C_{\text{rel}}^+ = C_{\text{rel}}/Re_\tau$, which is shown in figure 8b. The figure reveals similar qualitative trends to those in figure 8a: for small particles ($d_p = 25 \mu\text{m}$), increasing Re_τ enhances the wall concentration, whereas for larger particles ($d_p \geq 50 \mu\text{m}$) the concentration decreases with increasing Reynolds number. The latter trend is consistent with the observations of Bernardini (2014), while the increase in concentration for $d_p = 25 \mu\text{m}$ was not reported in their study, as they considered only $St \geq 1$. Moreover, the expected collapse for $10 \lesssim St \lesssim 25$ is not observed here. This deviation may be attributed to 4-way coupling and higher particle concentrations, in contrast to the 1-way coupled configuration of Bernardini (2014). The decrease in near-wall concentration with increasing Reynolds number can be due to a smaller turbophoretic drift as the fraction of inner layer to channel height decreases.

Figure 8c shows the charging behaviour for different Reynolds numbers, where the temporal evolution of the charge is plotted in seconds. For all particle sizes, an increase in Reynolds number leads to a higher charging rate, which is in accordance with experimental (Schwindt *et al.* 2017; Nifuku & Katoh 2003) and numerical observations (Grosshans & Papalexandris 2017b; Watano *et al.* 2003; Ceresiat *et al.* 2019). This effect is most pronounced for the smallest particles ($d_p = 25 \mu\text{m}$), where the charging rate increases

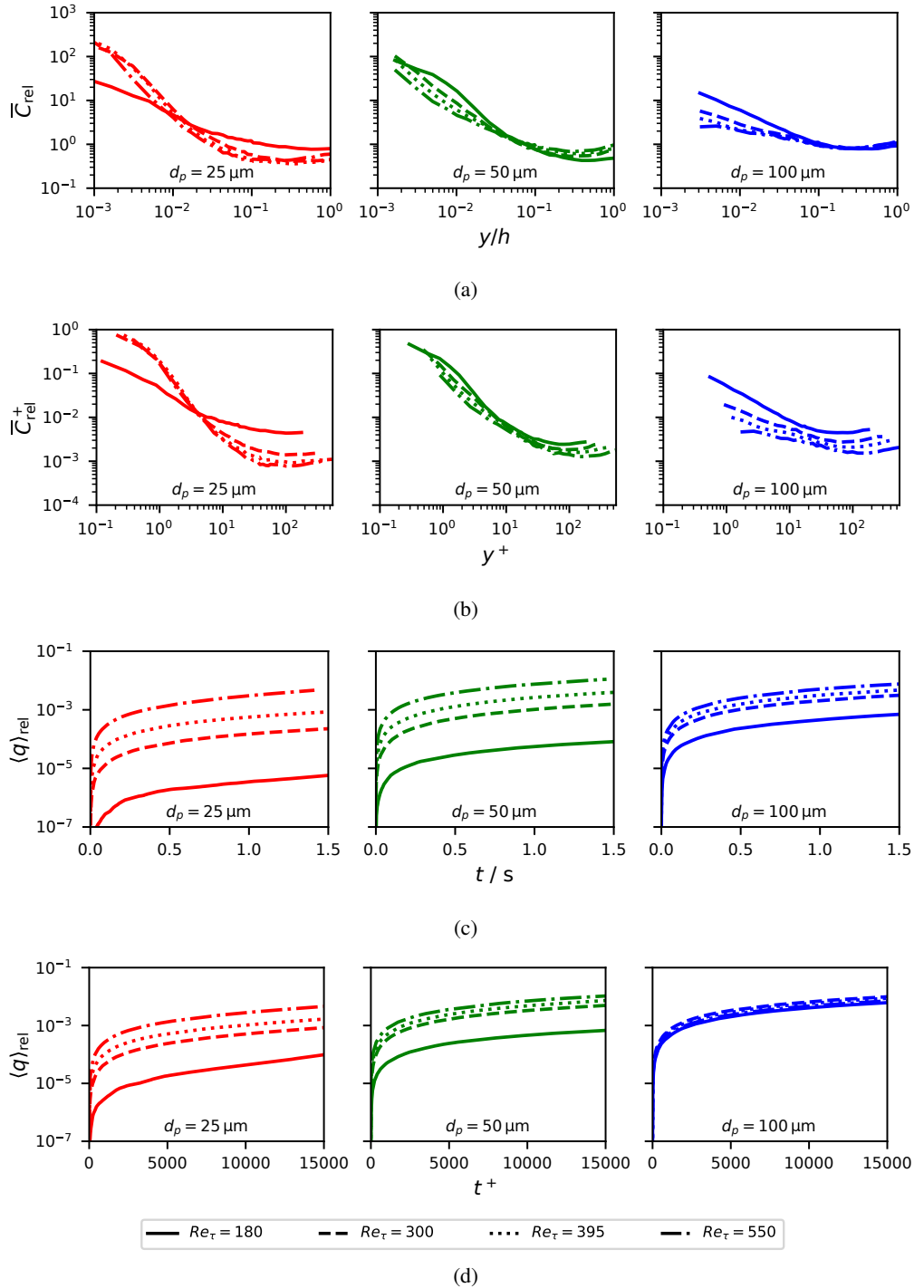


Figure 8. LES for particles of different sizes and friction Reynolds numbers. Relative density of uncharged particles C_{rel} plotted over wall-normal coordinate (a) in outer units and (b) inner/wall units. Averaged relative particle charge $\langle q \rangle_{\text{rel}}$ plotted over time in (c) seconds t and (d) wall units t^+ .

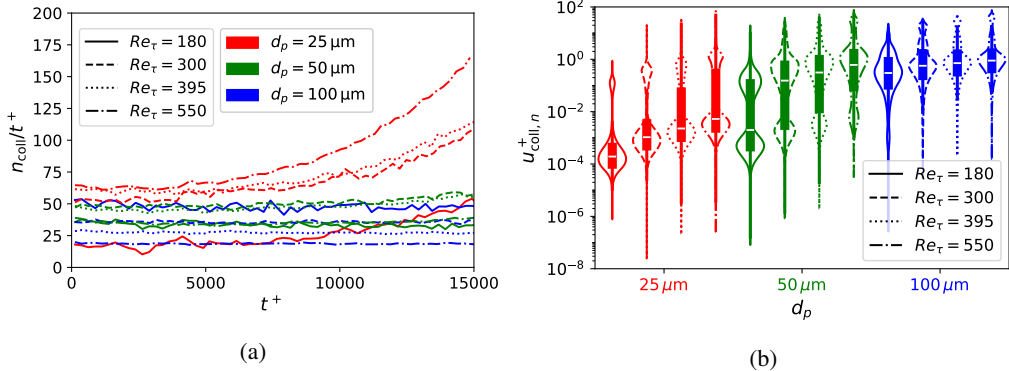


Figure 9. Four-way coupled LES for particles of different sizes and friction Reynolds numbers. (a) Particle collision rate n_{coll}/t^+ . (b) Distribution of the wall-normal collision velocity $u_{\text{coll},n}^+$.

by approximately two orders of magnitude as Re_τ rises from 180 to 550. For the largest particles ($d_p = 100 \mu\text{m}$), the effect is weaker, with only about one order of magnitude increase in charging rate. As a result, the highest charging rate is observed for medium-sized particles ($d_p = 50 \mu\text{m}$) at $Re_\tau = 550$. When the charge is plotted over wall units, t^+ , as shown in figure 8d, an asymptotic behaviour with increasing Re_τ becomes apparent, particularly for the larger particles. This tendency may facilitate the prediction of the charging rate at higher Reynolds numbers. However, the scaling appears to depend on particle size, as no collapse is observed for the smaller particles. Verification at higher Reynolds numbers is therefore required as this concept has not been previously reported in the literature.

To further assess the influence of Reynolds number on particle charging, figure 9 shows the particle–wall collision rate and the corresponding collision velocity. In agreement with the trends in figure 7, smaller particles exhibit an increase in collision frequency and charging rate over time (the latter not shown). These increases become stronger for higher Reynolds numbers. As discussed above, the enhanced collision rate is associated with recurring particle–wall interactions driven by the image charge force. A possible explanation for the Reynolds-number dependence is the higher collision velocity at larger Reynolds numbers, which accelerates particle charging and thus strengthens the image charge and the resulting electrostatic attraction towards the wall. In addition, the increased grid resolution relative to the particle diameter resolves steeper gradients of the electric potential. The relative contribution of these effects cannot be isolated on the basis of the present results. For the largest particles ($d_p = 100 \mu\text{m}$), the collision rate per unit wall time decreases with increasing Reynolds number. This trend is consistent with the reduced near-wall particle concentration observed at higher Reynolds numbers, an effect that is particularly pronounced for large particles.

The mean collision velocity increases with Reynolds number for all particle sizes, with the strongest increase for the smallest particles. The increased momentum of large-scale turbulent eddies for higher Reynolds numbers transports particles towards the wall. For particles with diameters of $d_p = 25 \mu\text{m}$ and especially for $50 \mu\text{m}$, a shift in the collision statistics from low-velocity to high-velocity impacts is observed with increasing Reynolds number. This shift aligns with the increase in turbulence intensity at higher Reynolds numbers. Stronger sweeps reduce particle residence times in the near-wall region, thereby suppressing low-velocity grazing collisions.

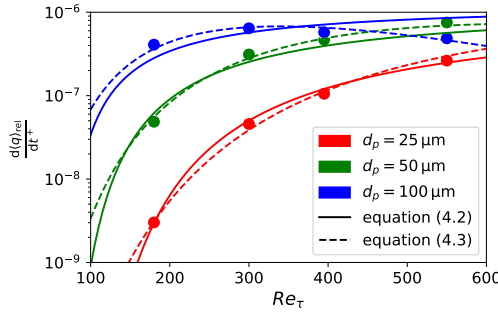


Figure 10. Correlation between friction Reynolds number and average charging rate $d\langle q \rangle_{\text{rel}}/dt$ for different particle sizes.

As a final step, figure 10 shows the charging rate as a function of Re_τ for the different particle sizes. In general, the charging rate exhibits a temporal evolution, most notably for small particles, for which a gradual increase is observed over time (see figure 4b). To eliminate this transient effect, the analysis is restricted to $t^+ < 4000$, where the charging rate is approximately constant for all cases. Consequently, the extracted charging rates exclude the influence of enhanced collision frequencies caused by image-charge-induced recurring collisions, as well as particle saturation effects that become relevant at later times.

According to Ozler & Grosshans (2025), the charging rate reduces once the mean particle charge reaches approximately 20–40 % of the saturation charge, q_{sat} . The influence of increased collision rates is confined to charge levels below approximately 10 %, q_{sat} , since particles undergoing recurring collisions have already approached saturation. As a result, the charging rates reported here are expected to overpredict the charge accumulation when extrapolated towards q_{sat} . All charging rates are determined on a temporal basis expressed in wall units, as the asymptotic behaviour is observed most clearly in this scaling. Overall, an increase in both Re_τ and particle diameter d_p leads to a higher charging rate per unit of t^+ . However, the tendency towards an asymptotic, Reynolds-number-independent charging rate becomes more pronounced with increasing particle size. For the largest particles considered ($d_p = 100 \mu\text{m}$), the charging rate even decreases for $Re_\tau > 300$.

To quantify these trends and to enable predictive estimates for other configurations, we propose two empirical relations obtained using symbolic regression (Cranmer 2023), namely

$$\log_{10} \left(\frac{d\langle q \rangle_{\text{rel}}}{dt^+} \right) = -5.89 - \frac{9070}{d_{p,\text{rel}} (Re_\tau - 42.5)} \quad (4.2)$$

and

$$\log_{10} \left(\frac{d\langle q \rangle_{\text{rel}}}{dt^+} \right) = -2.18 \cdot 10^{-5} Re_\tau d_{p,\text{rel}} - 4.64 - \frac{30360}{Re_\tau (d_{p,\text{rel}} + 4.92) + 2668} \quad (4.3)$$

with $d_{p,\text{rel}} = d_p/(50\delta)$. Equation (4.2) provides a compact representation of the charging-rate dependence at the expense of a slightly increased fitting error, whereas equation (4.3) yields a more accurate description, but at the cost of increased complexity. The difference between the two formulations lies in their behaviour at large Reynolds numbers. While Equation (4.2) predicts an asymptotic approach towards a maximum charging rate of approximately $\frac{d\langle q \rangle_{\text{rel}}}{dt^+} \approx 10^{-6} \text{C}$, equation (4.3) captures the reduction in charging rate observed for large particles at high Reynolds numbers. A careful extrapolation of equation (4.3) towards higher Reynolds numbers suggests a similar decrease for smaller

particles as well. Based on this formulation, the maximum charging rate is predicted to occur for particles with $d_p = 25 \mu\text{m}$ at $Re_\tau \approx 1280$, for $d_p = 50 \mu\text{m}$ at $Re_\tau \approx 665$, and for $d_p = 100 \mu\text{m}$ at $Re_\tau \approx 340$. Beyond these Reynolds numbers, the charging rate decreases again. Since these Reynolds numbers are relevant to a wide range of industrial applications, the underlying mechanisms responsible for this non-monotonic behaviour warrant further investigation.

The present investigation was initially motivated by contradictory trends reported in the literature regarding the Reynolds-number dependence of particle charging. The results presented here are consistent with recent numerical findings by Grosshans & Papalexandris (2017b) and with the experimental observations of Schwindt *et al.* (2017), both of which report an increase in particle charge with increasing Reynolds number. Furthermore, the results support the conclusions of Jantač & Grosshans (2024), who demonstrated that particle trajectories are strongly influenced by turbulent flow structures that intensify with increasing Reynolds number, leading to higher particle–wall impact velocities and, consequently, enhanced charging rates. In contrast, the simulations of Tanoue *et al.* (2001) and Watano (2006) do not resolve small-scale turbulent fluctuations, which provides a plausible explanation for the differing trends reported in those studies.

5. Conclusion

We presented the new CFD-DEM code triboFoam to simulate triboelectric charging in particle-laden flows. The code is based on the open-source library OpenFOAM, enabling parallel simulations of complex geometries combined with many physical models and numerical schemes. In the first step, triboFoam has been validated by DNS of a turbulent channel flow versus the open-source particle tracking library pafIX. The results show an excellent agreement between both codes for the fluid statistics as well as the particle distribution. Concerning the charging, a match could be obtained by selecting appropriate grid resolutions and time step sizes. In this study, we could see that triboFoam is stable in terms of grid and time step size variations. Moving forward, we extended triboFoam to LES of turbulent channel flows at different friction Reynolds numbers Re_τ ranging from 180 to 550 and three different particle sizes $d_p = 25 \mu\text{m}$, $50 \mu\text{m}$, and $100 \mu\text{m}$. The validation of the LES model highlighted how sensitive the particle kinematics are to turbulent flow and that the smallest eddies significantly contribute to a higher charging rate. The results concerning different Reynolds numbers show that with increasing Reynolds number the particle–wall collision velocity increases leading to a higher charging rate. Furthermore, smaller particles are more affected by the increase in Reynolds number as they follow the turbulent structures better being transported towards the wall with higher velocities. In addition, we observed for the small particles that with increasing Reynolds number the particle–wall collision frequency increases due to recurring collisions driven by the image charge force. Finally, we derived two versions of an empirical correlation for the average charging rate as a function of friction Reynolds number and particle size. These show that the normalised charging rate tends either asymptotically towards a maximum value or even decreases again for high Reynolds numbers. This behaviour should be investigated in future studies, as these Reynolds numbers are relevant for industrial applications.

REFERENCES

ABE, HIROYUKI, ANTONIA, ROBERT ANTHONY & KAWAMURA, HIROSHI 2009 Correlation between small-scale velocity and scalar fluctuations in a turbulent channel flow. *Journal of Fluid Mechanics* **627**, 1–32.

APODACA, M., WESSON, P., BISHOP, K., RATNER, M. & GRZYBOWSKI, B. 2019 Contact electrification between identical materials. *Angewandte Chemie International Edition* **49**, 946.

BERNARDINI, MATTEO 2014 Reynolds number scaling of inertial particle statistics in turbulent channel flows. *Journal of Fluid Mechanics* **758**.

BIANCO, F., CHIBBARO, SERGIO, MARCHIOLI, CRISTIAN, SALVETTI, MARIA V. & SOLDATI, ALFREDO 2012 Intrinsic filtering errors of lagrangian particle tracking in LES flow fields. *Physics of Fluids* **24** (4).

CERESIAT, LISE, GROSSHANS, HOLGER & PAPALEXANDRIS, MILTADIS V. 2019 Powder electrification during pneumatic transport: The role of the particle properties and flow rates. *Journal of Loss Prevention in the Process Industries* **58**, 60–69.

CRANNER, MILES 2023 Interpretable Machine Learning for Science with PySR and SymbolicRegression.jl. ArXiv:2305.01582 [astro-ph, physics:physics].

CROWE, CLAYTON T., SCHWARZKOPF, JOHN D., SOMMERFELD, MARTIN & TSUJI, YUTAKA 2011 *Multiphase Flows with Droplets and Particles*. CRC Press.

CUI, YUANKAI, ZHANG, HUAN & ZHENG, XIAOJING 2024 Turbulence modulation by charged inertial particles in channel flow. *Journal of Fluid Mechanics* **990**.

FATH, WOLFGANG, BLUM, CARSTEN, GLOR, MARTIN & WALTHER, CLAUS-DIETHER 2013 Electrostatic ignition hazards due to pneumatic transport of flammable powders through insulating or dissipative tubes and hoses – New experiments and calculations. *Journal of Electrostatics* **71** (3), 377–382.

FORWARD, KEITH M., LACKS, DANIEL J. & SANKARAN, R. MOHAN 2009 Charge segregation depends on particle size in triboelectrically charged granular materials. *Physical Review Letters* **102** (2).

GIFFIN, AMANDA & MEHRANI, POUPAK 2013 Effect of gas relative humidity on reactor wall fouling generated due to bed electrification in gas-solid fluidized beds. *Powder Technology* **235**, 368–375.

GLOR, M. 1985 Hazards due to electrostatic charging of powders. *Journal of Electrostatics* **16** (2–3), 175–191.

GLOR, MARTIN 2001 Overview of the occurrence and incendivity of cone discharges with case studies from industrial practice. *Journal of Loss Prevention in the Process Industries* **14** (2), 123–128.

GROSJEAN, GALIEN & WAITUKAITIS, SCOTT 2023a Asymmetries in triboelectric charging: Generalizing mosaic models to different-material samples and sliding contacts. *Physical Review Materials* **7**, 065601.

GROSJEAN, GALIEN & WAITUKAITIS, SCOTT 2023b Single-collision statistics reveal a global mechanism driven by sample history for contact electrification in granular media. *Physical Review Letters* **130** (9).

GROSSHANS, HOLGER, WILMS, CHRISTOPH, JANTAČ, SIMON, OBUKOHWO, OTOME & ÖZLER, GIZEM 2026 pafix - particle flow simulation in explosion protection.

GROSSHANS, HOLGER, ÖZLER, GIZEM, VEERAVALLI, VYSHNAVI & JANTAČ, SIMON 2025 Unifying same- and different-material particle charging through stochastic scaling. *Physical Review X*.

GROSSHANS, HOLGER & PAPALEXANDRIS, MILTADIS V. 2016a Evaluation of the parameters influencing electrostatic charging of powder in a pipe flow. *Journal of Loss Prevention in the Process Industries* **43**, 83–91.

GROSSHANS, HOLGER & PAPALEXANDRIS, MILTADIS V. 2016b Large eddy simulation of triboelectric charging in pneumatic powder transport. *Powder Technology* **301**, 1008–1015.

GROSSHANS, HOLGER & PAPALEXANDRIS, MILTADIS V. 2017a Direct numerical simulation of triboelectric charging in a particle-laden turbulent channel flow. *Journal of Fluid Mechanics* **818**, 465–491.

GROSSHANS, HOLGER & PAPALEXANDRIS, MILTADIS V. 2017b A model for the non-uniform contact charging of particles. *Powder Technology* **305**, 518–527.

GROSSHANS, HOLGER & PAPALEXANDRIS, MILTADIS V. 2017c On the accuracy of the numerical computation of the electrostatic forces between charged particles. *Powder Technology* **322**, 185–194.

IWAMOTO, KAORU, SUZUKI, YUJI & KASAGI, NOBUHIDE 2002 Reynolds number effect on wall turbulence: toward effective feedback control. *International Journal of Heat and Fluid Flow* **23** (5), 678–689.

JANTAČ, SIMON & GROSSHANS, HOLGER 2024 Suppression and control of bipolar powder charging by turbulence. *Physical Review Letters* **132** (5).

JIN, X. & MARSHALL, J. S. 2017 The role of fluid turbulence on contact electrification of suspended particles. *Journal of Electrostatics* **87**, 217–227.

JOHN, WALTER, REISCHL, GEORGE & DEVOR, W. 1980 Charge transfer to metal surfaces from bouncing aerosol particles. *Journal of Aerosol Science* **11** (2), 115–138.

JONES, MARK 1997 *Pneumatic Conveying*, p. 378–388. Springer US.

KLINZING, G. E. 2018 A review of pneumatic conveying status, advances and projections. *Powder Technology* **333**, 78–90.

KOREVAAR, MARTIN W., PADDING, JOHAN T., VAN DER HOEF, MARTIN A. & KUIPERS, J.A.M. 2014 Integrated dem-cfd modeling of the contact charging of pneumatically conveyed powders. *Powder Technology* **258**, 144–156.

KUERTEN, J. G. M. 2016 Point-particle dns and les of particle-laden turbulent flow - a state-of-the-art review. *Flow, Turbulence and Combustion* **97** (3), 689–713.

KUERTEN, J. G. M. & VREMAN, A. W. 2004 Can turbophoresis be predicted by large-eddy simulation? *Physics of Fluids* **17** (1), 011701–011701–4.

LACKS, DANIEL J., DUFF, NATHAN & KUMAR, SANAT K. 2008 Nonequilibrium accumulation of surface species and triboelectric charging in single component particulate systems. *Physical Review Letters* **100**, 188305.

LACKS, D. J. & LEVANDOVSKY, A. 2007 Effect of particle size distribution on the polarity of triboelectric charging in granular insulator systems. *Journal of Electrostatics* **65**, 107–112.

LEE, MYOUNGKYU & MOSER, ROBERT D. 2015 Direct numerical simulation of turbulent channel flow up to. *Journal of Fluid Mechanics* **774**, 395–415.

LI, JINZHUI, YAO, JUN, ZHAO, YANLIN & WANG, CHI-HWA 2021 Large eddy simulation of electrostatic effect on particle transport in particle-laden turbulent pipe flows. *Journal of Electrostatics* **109**, 103542.

LIM, ELDIN WEE CHUAN, ZHANG, YAN & WANG, CHI-HWA 2006 Effects of an electrostatic field in pneumatic conveying of granular materials through inclined and vertical pipes. *Chemical Engineering Science* **61** (24), 7889–7908.

LOWELL, J. & TRUSCOTT, I. 1986a Triboelectrification of identical insulators. I. An experimental investigation. *Journal of Physics D: Applied Physics* **19**, 1273.

LOWELL, J. & TRUSCOTT, I. 1986b Triboelectrification of identical insulators. II. Theory and further experiments. *Journal of Physics D: Applied Physics* **19**, 1281.

MARCHIOLI, CRISTIAN, SALVETTI, MARIA V. & SOLDATI, ALFREDO 2008 Some issues concerning large-eddy simulation of inertial particle dispersion in turbulent bounded flows. *Physics of Fluids* **20** (4), 040603.

MATSUYAMA, TATSUSHI 2018 A discussion on maximum charge held by a single particle due to gas discharge limitation. In *AIP Conference Proceedings*, , vol. 1927, p. 020001. Author(s).

MATSUYAMA, TATSUSHI, OGU, MASAOMI, YAMAMOTO, HIDEO, MARINISSEN, JAN C.M & SCARLETT, BRIAN 2003 Impact charging experiments with single particles of hundred micrometre size. *Powder Technology* **135–136**, 14–22.

NICLOUD, FRANCK & DUCROS, FRÉDÉRIC 1999 Subgrid-scale stress modelling based on the square of the velocity gradient tensor. *Flow, Turbulence and Combustion* **62** (3), 183–200.

NIFUKU, MASAHIRO & KATO, HIROMI 2003 A study on the static electrification of powders during pneumatic transportation and the ignition of dust cloud. *Powder Technology* **135–136**, 234–242.

OSHAWA, A. 2011 Statistical analysis of fires and explosions attributed to static electricity over the last 50 years in Japanese industry. *Journal of Physics: Conference Series* **301**, 012033.

OZLER, GIZEM & GROSSHANS, HOLGER 2025 Secondary flows drive triboelectric powder charging in pneumatic conveying. *Journal of Fluid Mechanics* **1007**.

RUPP, DAVID A., MORTIMER, LEE F. & FAIRWEATHER, MICHAEL 2023 Stokes number and coupling effects on particle interaction behavior in turbulent channel flows. *Physics of Fluids* **35** (11).

SARDINA, GAETANO, PICANO, FRANCESCO, SCHLATTER, PHILIPP, BRANDT, LUCA & CASCIO, CARLO M. 2013 Statistics of particle accumulation in spatially developing turbulent boundary layers. *Flow, Turbulence and Combustion* **92** (1–2), 27–40.

SARDINA, GAETANO, SCHLATTER, PHILIPP, BRANDT, LUCA, PICANO, FRANCESCO & CASCIO, CARLO M. 2012 Wall accumulation and spatial localization in particle-laden wall flows. *Journal of Fluid Mechanics* **699**, 50–78.

SCHILLER, LUDWIG & NAUMANN, ALEXANDER 1933 A drag coefficient correlation. *Z. Vereines Deutscher Inge.* **77**, 318–320.

SCHWINDT, N., von PIDOLL, ULRICH, MARKUS, DETLEV, KLAUSMEYER, UWE, PAPALEXANDRIS, M.V. & GROSSHANS, HOLGER 2017 Measurement of electrostatic charging during pneumatic conveying of powders. *Journal of Loss Prevention in the Process Industries* **49**, 461–471.

SHAW, PHILIP E. & JEX, C. S. 1928 Tribo-electricity and friction. III. – Solid elements and textiles. *Proceedings of the Royal Society of London. Series A, Containing Papers of a Mathematical and Physical Character* **118** (779), 108–113, arXiv: <https://royalsocietypublishing.org/doi/pdf/10.1098/rspa.1928.0038>.

SMAGORINSKY, JOSEPH 1963 General circulation experiments with the primitive equations: I. the basic experiment. *Monthly Weather Review* **91** (3), 99–164.

SOO, SHAO L. 1971 Dynamics of charged suspensions. In *Topics in Current Aerosol Research* (ed. G.M. HIDY & J.R. BROCK), *International Reviews in Aerosol Physics and Chemistry* 1, p. 61. Pergamon.

TANOU, KEN-ICHIRO, TANAKA, HIROSHI, KITANO, HAJIME & MASUDA, HIROAKI 2001 Numerical simulation of tribo-electrification of particles in a gas–solids two-phase flow. *Powder Technology* **118** (1–2), 121–129.

VREMAN, A. W. & KUERTEN, J. G. M. 2014 Comparison of direct numerical simulation databases of turbulent channel flow at $Re_\tau = 180$. *Physics of Fluids* **26** (1).

WATANO, SATORU 2006 Mechanism and control of electrification in pneumatic conveying of powders. *Chemical Engineering Science* **61** (7), 2271–2278.

WATANO, SATORU, SAITO, SEIJI & SUZUKI, TERUO 2003 Numerical simulation of electrostatic charge in powder pneumatic conveying process. *Powder Technology* **135–136**, 112–117.

WELLER, HENRY G., TABOR, GAVIN, JASAK, HRVOJE & FUREBY, CHRISTER 1998 A tensorial approach to computational continuum mechanics using object-oriented techniques. *Computers in Physics* **12** (6), 620–631.

WILMS, CHRISTOPH & GROSSHANS, HOLGER 2026 triboFoam – An open-source CFD solver for triboelectric charging of particles.

WON-WOOK, KIM & SURESH, MENON 1995 *A new dynamic one-equation subgrid-scale model for large eddy simulations*, chap. 356, pp. 1–9. American Institute of Aeronautics and Astronautics Inc., arXiv: <https://arc.aiaa.org/doi/pdf/10.2514/6.1995-356>.

YAN, YUDONG, ZHAO, YANLIN, YAO, JUN & WANG, CHI-HWA 2021 Investigation of particle transport by a turbulent flow through a 90° bend pipe with electrostatic effects. *Powder Technology* **394**, 547–561.

YOSHIZAWA, AKIRA 1986 Statistical theory for compressible turbulent shear flows, with the application to subgrid modeling. *The Physics of Fluids* **29** (7), 2152–2164.

ZHANG, GAOQIANG, MENG, HE, LI, YIPENG, ZHOU, QUN, SU, ZHAOXING & LIANG, CAI 2026 Electrostatic risk assessment in industrial-scale silos incorporating the coupled effects of powder charging and conveying parameters. *Powder Technology* **468**, 121661.

ZHANG, HUAN, CUI, YUANKAI & ZHENG, XIAOJING 2023 How electrostatic forces affect particle behaviour in turbulent channel flows. *Journal of Fluid Mechanics* **967**.

Funding This work received financial support from the European Research Council (ERC) under the European Union’s Horizon 2020 research and innovation programme (Grant Agreement No. 947606, Pow-FEct). The authors gratefully acknowledge the computing time made available to them on the high-performance computer “Lise” at the NHR centre NHR@ZIB. This centre is jointly supported by the Federal Ministry of Education and Research and the state governments participating in the NHR (www.nhr-verein.de).

Acknowledgement Additional computational resources were provided by the PTB cluster, which the authors also gratefully acknowledge. In addition, the authors like to thank Jiri Polansky from ESI-OpenCFD for his valuable feedback during the implementation of triboFoam in the OpenFOAM framework.

Declaration of Interests The authors report no conflict of interest.

Data availability statement The data in the present manuscript will be made available upon request.

Use of artificial intelligence tools The authors used ChatGPT v5.2 solely for the purpose of language editing and grammatical refinement to improve the readability of the manuscript. All scientific content, data analysis, and conclusions were developed exclusively by the human authors, who remain fully accountable for the accuracy, integrity, and originality of the work

Appendix A. DNS: Grid and time step study

This subsection evaluates the influence of grid resolution in the wall-normal direction and the time step length. Figure 11a compares three grid resolutions, 144, 244, and 344 cells in the wall-normal direction, in terms of particle charging over time. The meshes are identical for pafiX and triboFoam. triboFoam exhibits stable behaviour with respect to grid variations for both particle sizes. In contrast, pafiX shows an increased charging rate for small particles of $d_p = 25 \mu\text{m}$ at higher grid resolutions due to a higher particle-wall collision rate and velocity. For larger particles of $d_p = 100 \mu\text{m}$, no significant dependence on grid resolution is observed, indicating that smaller Stokes numbers are more sensitive to grid resolution. Figure 11b illustrates the influence of time step length on particle charging. Again, triboFoam demonstrates stable behaviour with a slight increase in charging rate. In contrast, pafiX exhibits a noticeable increase in charging rate for all particle sizes with decreasing time step size. An increase in charging rate is reasonable as it resolves higher particle-wall collision frequencies.

To investigate this in more detail, and as the time step length has a more significant effect on the charging behaviour than the grid resolution, figure 12 shows the mean particle-wall collision frequency and the distribution of wall-normal particle collision velocity for different time step lengths. It can be seen that with decreasing time step length, the mean particle-wall collision frequency increases for both solvers. However, triboFoam shows for the large particles almost no change and for the medium sized particles the biggest change with about 0.7 orders of magnitude. In contrast, pafiX shows a more consistent increase in collision frequency with decreasing time step length for all particle sizes in the range of 3 to 4 orders of magnitude. This suggests that triboFoam is less sensitive to time step length variations for larger particles compared to pafiX. In the very

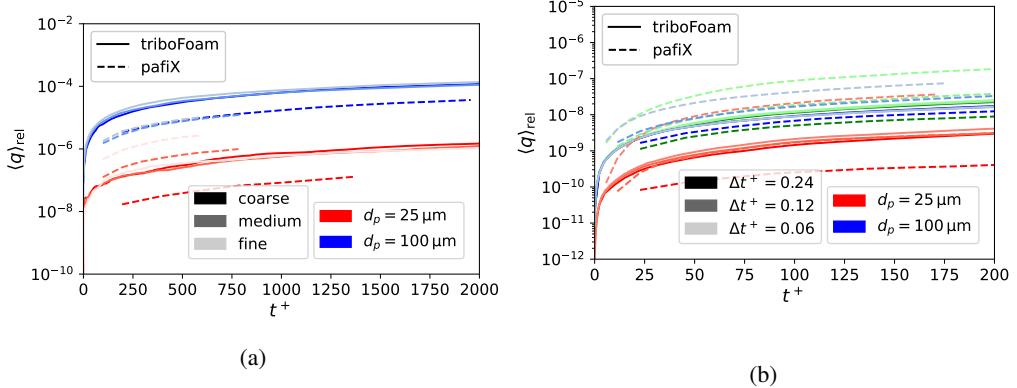


Figure 11. Averaged relative particle charge \bar{q}_{rel} over time for both solvers and two different particle sizes. Compared are in (a) different grid resolutions and in (b) different time step sizes. DNS of $Re_\tau = 180$, the particles are 1-way coupled to the fluid.

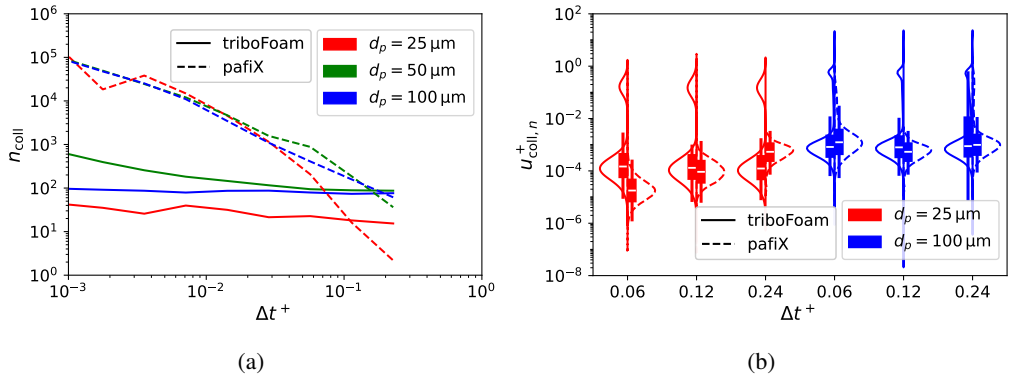


Figure 12. Effect of time step size on (a) the mean particle-wall collision frequency and (b) the distribution of wall-normal particle collision velocity $u_{\text{coll},n}^+$ for DNS of $Re_\tau = 180$.

end, a realistic collision frequency needs to be determined based on experiments to choose an appropriate time step length for the simulations. The effect of the time step length on the collision velocity is depicted in figure 12. For the particle size of $d_p = 100 \mu\text{m}$, no significant trend can be observed for both solvers. However, for the small particle size, trifoam, again, shows almost no change with varying time step lengths, while pafix shows a trend towards lower collision velocities with decreasing time step lengths. In addition, both solvers differ in general in the distribution of the collision velocities, with trifoam showing a bimodal distribution with low and high speed collisions and pafix a more Gaussian distribution with the low speed collisions. Similar to the collision frequency, this has to be further investigated based on experimental data to choose an appropriate time step length for the simulations.

Appendix B. LES: Comparison of closure models

Four different LES closure models were compared against a reference DNS: Smagorinsky, k -equation (kEqn), dynamic k -equation (dykEqn), and wall-adapting local eddy-viscosity (WALE). The comparison was carried out at $Re_\tau = 180$ using the smallest particle size, which is most sensitive to variations in the fluid field. The grid corresponds to the medium resolution described in Section C. Figure 13a presents the wall-normal velocity profiles for the different models. The kEqn model underpredicts the bulk velocity, which appears to result from a delayed onset and termination of the buffer layer. The other three models produce nearly identical profiles, slightly overpredicting the bulk velocity. Agreement with the DNS is very good up to $y^+ < 10$ (within 1%), but the velocity increases too rapidly beyond this region, indicating a delayed onset of the logarithmic layer. All

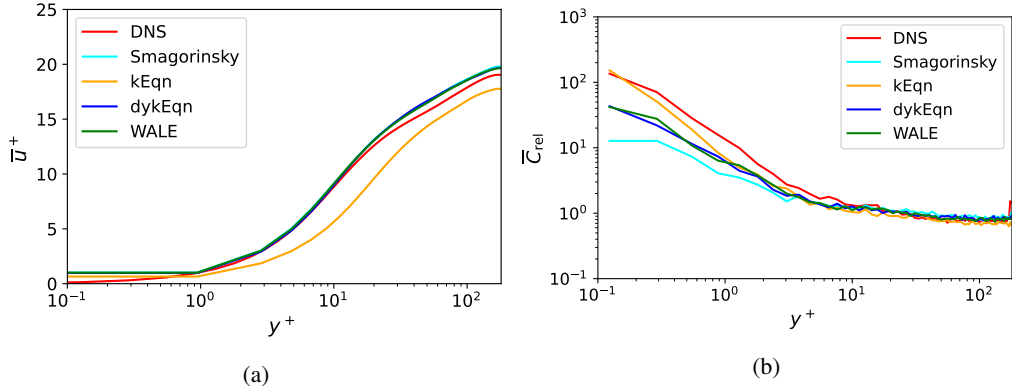


Figure 13. Effect of LES closure model on the velocity profile \bar{u}^+ and particle concentration \bar{C}_{rel} plotted over wall-normal distance y^+ . All simulations for $Re_\tau = 180$ with particles of a size with $d_p = 25\mu\text{m}$. The particles are 4-way coupled to the fluid.

LES models underestimate the velocity in the defect region ($y^+ > 0.3 Re_\tau$), though this is expected to have only a minor impact on the particle dynamics. Figure 13b compares the resulting particle concentration profiles. The kEqn model predicts the near-wall concentration most accurately, followed by the dykEqn and WALE models, which show nearly identical trends, while the Smagorinsky model yields the largest underprediction. Considering both the velocity and concentration profiles, the dykEqn and WALE models perform best overall. The WALE model was chosen for subsequent simulations, owing to its 16 % higher computational efficiency compared with the dykEqn model.

Appendix C. LES: Grid study

This section investigates the influence of grid resolution on the velocity and particle concentration profiles in order to validate the LES setup. The grid study compares three resolutions—referred to as *coarse*, *medium*, and *fine*—for friction Reynolds numbers $Re_\tau = 180, 300, 395$, and 550 . The respective wall-unit resolutions are $\Delta x^+ = 39.5$, $\Delta z^+ = 26.3$, $\Delta y_w^+ = 1.9$, and $\Delta y_w^+ = 12.5$ (coarse), $\Delta x^+ = 19.75$, $\Delta z^+ = 13.16$, $\Delta y_w^+ = 0.96$, and $\Delta y_w^+ = 6.25$ (medium), and $\Delta x^+ = 9.88$, $\Delta z^+ = 6.58$, $\Delta y_w^+ = 0.47$, and $\Delta y_w^+ = 6.25$ (fine). At higher Re_τ , additional grid variations were examined to reduce computational cost. The smallest particle size, $d_p = 25\mu\text{m}$, was chosen as it is most sensitive to the fluid field. DNS data at the corresponding Reynolds numbers serve as reference: in-house DNS for $Re_\tau = 180$ and 300 , and literature data for $Re_\tau = 395$ and 550 (Abe *et al.* 2009; Lee & Moser 2015). For the latter two cases, only the velocity profiles are compared since the DNS data are single-phase; however, the influence of four-way coupling on the mean velocity is expected to be minor due to the low particle concentration.

Figure 14a shows that, at $Re_\tau = 180$, the LES velocity profile approaches the DNS reference with increasing grid resolution. Coarser grids overpredict the bulk velocity, while all grids accurately capture the viscous sublayer. Beyond $y^+ > 10$, the velocity rises too rapidly, delaying the onset of the logarithmic layer; this discrepancy diminishes with increasing resolution, and the fine grid yields a maximum deviation below 1.7 %. The corresponding particle concentration profiles in figure 14b reveal a strong dependence on resolution. The coarsest grid underpredicts the near-wall concentration by more than an order of magnitude, while the fine grid closely reproduces the DNS reference with a maximum deviation of 35 %. These results highlight the sensitivity of turbophoretic particle transport to small-scale turbulent motions, consistent with the findings of Jantač & Grosshans (2024). Consequently, the *fine* grid is selected for LES at $Re_\tau = 180$.

At $Re_\tau = 300$, similar trends are observed. The velocity profile converges towards the DNS with increasing resolution, and the coarsest grid again overpredicts the bulk velocity, see figure 15a. From the medium resolution onwards, good agreement with the in-house DNS is achieved (within 1.6 %). The slightly higher velocities in the logarithmic region compared with the reference DNS of Iwamoto *et al.* (2002) are due to four-way coupling effects, whereby the particle phase transfers momentum to the fluid. The particle concentration remains more sensitive to grid resolution than the mean velocity, with the peak concentration differing by about 12 % between the DNS and the fine grid (figure 15b). Hence, the *fine* grid is selected for LES at $Re_\tau = 300$.

For higher Reynolds numbers ($Re_\tau = 395$ and 550), the same qualitative behaviour is observed, though the results become less sensitive to grid coarsening, see figure 16 and figure 17. This reduction in sensitivity

Re_τ	Δx^+	Δz^+	Δy_w^+	Δy_c^+
180	9.88	6.58	0.47	6.25
300	9.88	6.58	0.47	6.25
395	9.88	6.58	0.47	6.25
550	19.75	6.58	0.47	6.25

Table 3. Overview of the grid resolution parameters for LES.

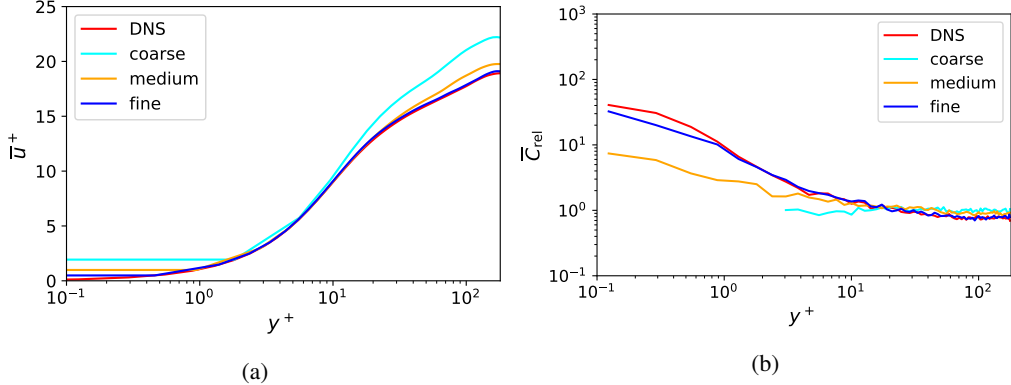


Figure 14. Effect of the LES grid resolution on the velocity profile \bar{u}^+ and particle concentration \bar{C}_{rel} plotted over wall-normal distance y^+ . All simulations are conducted at $Re_\tau = 180$ with particles of a size with $d_p = 25\mu\text{m}$. The particles are 4-way coupled to the fluid.

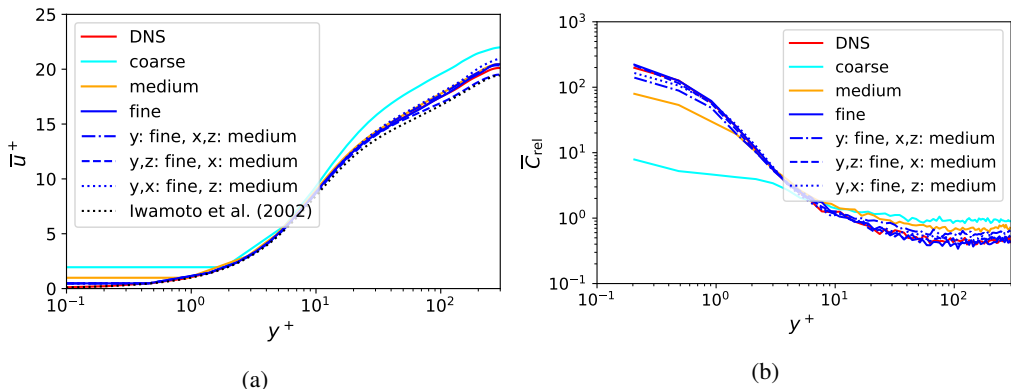


Figure 15. Effect of the LES grid resolution on the velocity profile \bar{u}^+ and particle concentration \bar{C}_{rel} plotted over wall-normal distance y^+ . All simulations are conducted at $Re_\tau = 300$ with particles of a size with $d_p = 25\mu\text{m}$. The particles are 4-way coupled to the fluid.

is attributed to the larger outer-scale resolution at higher Reynolds numbers, where the dominant turbulent structures are already well captured even on coarser grids. Moreover, LES is inherently more effective at higher Re_τ due to the broader range of turbulent scales. The final grid resolutions used in the Reynolds-number study presented in Section 4.4 are summarised in table 3.

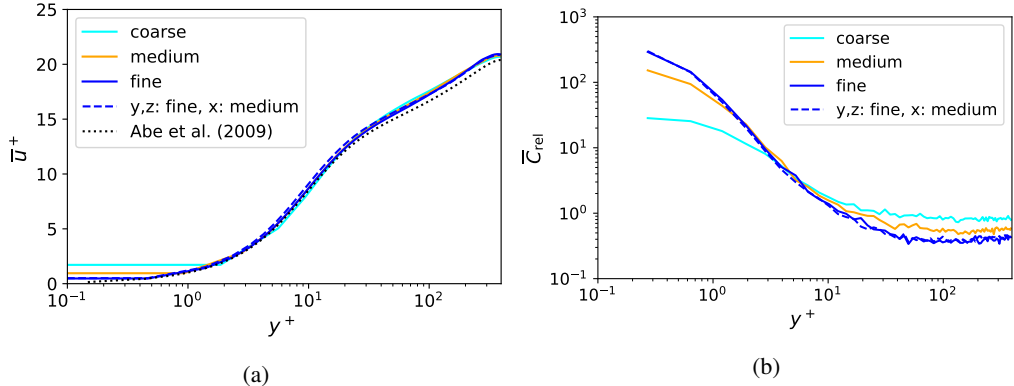


Figure 16. Effect of the LES grid resolution on the velocity profile \bar{u}^+ and particle concentration \bar{C}_{rel} plotted over wall-normal distance y^+ . All simulations are conducted at $Re_\tau = 395$ with particles of a size with $d_p = 25\mu\text{m}$. The particles are 4-way coupled to the fluid.

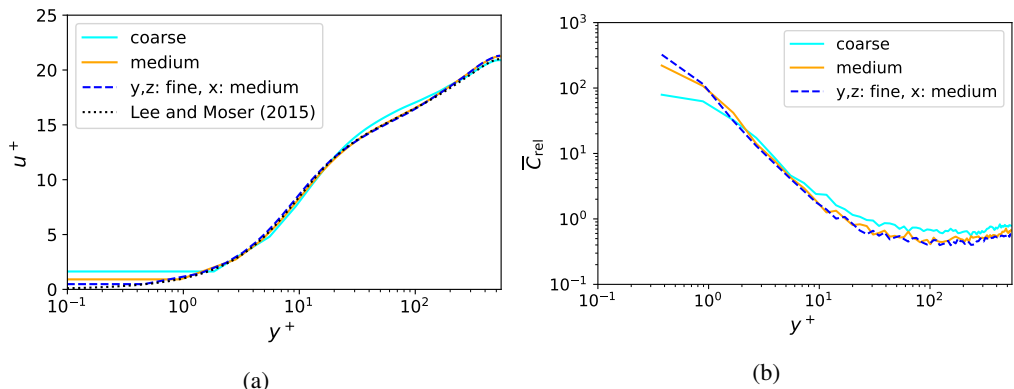


Figure 17. Effect of the LES grid resolution on the velocity profile \bar{u}^+ and particle concentration \bar{C}_{rel} plotted over wall-normal distance y^+ . All simulations are conducted at $Re_\tau = 550$ with particles of a size with $d_p = 25\mu\text{m}$. The particles are 4-way coupled to the fluid.

Appendix D. Comparison of condenser and stochastic scaling model

The SSM is able to predict a very similar charging behaviour as the condenser model by setting the parameters of the reference impact accordingly. Figure 18 depicts the particle charge plotted over the number of particle-wall collisions for both charging models and the three different particle sizes. Up to approximately 10^4 particle-wall collisions the models do not differ in the charge built-up. For the investigated time duration, no particles exceed that number of particle wall-collisions meaning that both charging models can predict the same charging behaviour. To obtain these results, the quantities of the reference impact need to be set in the following way: $\sigma_0 = \gamma_0 = 0$ and $\mu_0 = \Delta q_{0,\text{min}} = \mu_{\text{condenser}}$. $\mu_{\text{condenser}}$ is a function of u_n and d_p where $u_n = 0.01\text{ m s}^{-1}$ is a matches the average wall-normal particle impact velocity. For this constellation, particles of $d_p = 25\mu\text{m}$ require $\mu_{\text{condenser}} = 2.7702 \cdot 10^{-10}\text{ C}$, $d_p = 50\mu\text{m}$ require $\mu_{\text{condenser}} = 2.1417 \cdot 10^{-13}\text{ C}$ and $d_p = 100\mu\text{m}$ require $\mu_{\text{condenser}} = 7.7107 \cdot 10^{-15}\text{ C}$.

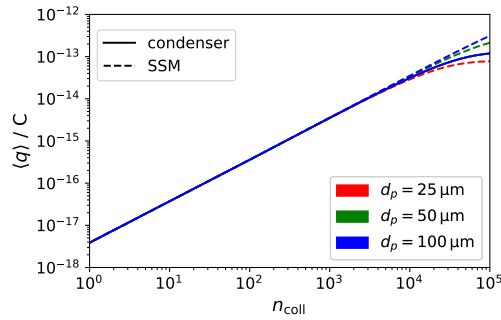


Figure 18. Comparison of the condenser model with a saturation charge of $q_{\text{sat}} = 1.23 \cdot 10^{13} \text{ C}$ and the SSM with $\sigma_0 = \gamma_0 = 0$ to reproduce the condenser model by setting $\mu_0 = \Delta q_{0,\text{min}} = \mu_{\text{condenser}}$. Plotted is the particle charge over the number of particle-wall collisions.